The Aeronautical Journal (2022), **126**, pp. 617–644
doi:10.1017/aer.2021.88

REGULAR PAPER

Investigation of rarefied flow over backward-facing step in different rarefaction regimes using direct simulation Monte Carlo

D. Nabapure, A. Singh and R.C.M. Kalluri

High-Performance Computing (HPC) Lab, Department of Mechanical Engineering, BITS-Pilani, Hyderabad Campus, 500078, India
E-mail: p20150056@hyderabad.bits-pilani.ac.in

Received: 19 June 2021; **Revised:** 7 September 2021; **Accepted:** 9 September 2021

Keywords: DSMC; Backward-facing step; Knudsen number; Rarefied gas flows

Abstract

Hypersonic aerothermodynamics for a re-entry vehicle approaching the earth's atmosphere is critical in the exploration of space. These vehicles often encounter various flow regimes due to the density variations and have surface abnormalities. The backward-facing step (BFS) is one such simplified configuration for modeling anomalies around such space vehicles. The present work examines rarefied hypersonic flow over a BFS using the direct simulation Monte Carlo (DSMC) method. The purpose of this research is focused on exploring the various loads encountered by a re-entry vehicle passing through different altitudes covering different rarefaction regimes. The fluid considered was non-reacting air, with the free-stream Mach number as 25, and the Knudsen number considered ranged from 0.05-21.10. The influence of the Knudsen number on flow characteristics has been elucidated graphically in various streamwise directions. The normalised flow properties such as velocity, pressure, temperature and density showed an increasing trend with the Knudsen number due to compressibility and viscous heating effects. In all flow regimes, there was an appearance of flow recirculation. With rarefaction, the recirculation lengths decreased, whereas the boundary layer thickness showed an increase. The aerodynamic surface properties such as pressure coefficient, skin friction, and heat transfer coefficient, by and large, showed an increase with the Knudsen number. When the chemical reactions were accounted for and compared against the non-reacting flows, the velocity, pressure, and density field showed no marked variation; however, considerable variations were observed in the temperature field. Furthermore, the present study also depicts the compressibility factor contour, showing the flow regions that diverge from the ideal gas behaviour.

Nomenclature

Abbreviations

BE	Boltzmann Equation
DSMC	Direct Simulation Monte Carlo
MD	Molecular Dynamics
NSF	Navier-Stokes Fourier
PPC	Particles Per Cell

Symbols

c'	Thermal velocity of the molecules [m/s]
C_p	Pressure coefficient
C_f	Skin friction coefficient
C_h	Heat transfer coefficient

d	Molecular diameter [m]
f	Distribution function
h	Characteristic length-(Step height) [m]
H	Channel height at outlet [m]
k_b	Boltzmann constant
Kn	Knudsen Number
m	Molecular mass [kg]
M	Mach Number
n	Number density [m^{-3}]
N	Number of molecules
P	Pressure [N/m^2]
q	Heat flux [W/m^2]
R	Gas constant [J/mol. K]
Re	Reynolds Number
t	Time [s]
T	Temperature [K]
X	Distance in x-direction [m]
Y	Distance in y-direction [m]

Greek Symbols

χ	Mole fraction
ω	Viscosity-temperature index
ρ	Density of the gas [kg/m^3]
μ	Viscosity of the gas [$N.s/m^2$]
τ	Shear stress [N/m^2]
λ	Mean free path [m]
ς	Degree of freedom
Δ	Timestep
Θ	Vibrational temperature
δ	Boundary layer thickness

Subscripts

∞	Free stream
s	Slip
j	Jump
w	Wall
R	Rotational
T	Translational
V	Vibrational
ov	Overall

1.0 Introduction

The aerospace vehicles that enter the earth from outer space require extensive research in rarefied gas flow dynamics. Generally, such vehicles operate at hypersonic speeds (Mach number of above 5), at higher altitudes, and encounter a rarefied flow environment. Furthermore, they usually experience different rarefaction regimes, ambient temperatures, and intricate flow patterns, including shocks [1]. Also, the chemical reactions at higher altitudes influence the flow field properties [2]. While it is desirable to have a smooth aerodynamic surface shape, several irregularities exist on such vehicles in the form of steps, contours, gaps during their development stage or flight. These abnormalities arise due to sensor installations, manufacturing tolerances and the placement of thermal protection system tiles [3]. Such abnormalities in advanced aerodynamic configurations lead to flow separation [4, 5]. The backward-facing step (BFS) is one of such simplified irregularities, which is mainly explored. The investigation

https://doi.org/10.1017/aer.2021.88 Published online by Cambridge University Press

into the BFS flow also has many practical applications in various fields [6]. Therefore, in this paper, the rarefaction effects on the flow behaviour past a BFS are addressed. The Knudsen number (Kn) is employed to estimate the flow rarefaction and is given by [7].

$$Kn = \frac{\lambda}{\mathrm{h}} \tag{1}$$

where, λ depicts the mean free path, and h is the characteristic dimension of the geometry under consideration. In the present work, h is the step height.

The Knudsen number classifies the flow regimes as [8]: $Kn \leq 0.001$ (Continuum regime), $0.001 \leq Kn \leq 0.1$ (Slip regime), $0.1 \leq Kn \leq 10$ (Transitional regime) and $Kn \geq 10$ (free-molecular regime). The breakdown of continuum theory occurs as the flow approaches the slip regime owing to prevalent rarefaction results, thereby requiring the use of computational alternatives, such as the solution of Boltzmann equations (BE), direct simulation Monte Carlo (DSMC), and Molecular dynamics (MD).

The Knudsen number (Kn), Reynolds number (Re) , and Mach number (M) are related to each other as follows:

$$Kn = \sqrt{\frac{\pi\gamma}{2}}\frac{\mathrm{M}}{\mathrm{Re}} \text{ where } \mathrm{M} = \frac{U_\infty}{\sqrt{\gamma RT}} \text{ and } \mathrm{Re} = \frac{\rho U_\infty h}{\mu} \tag{2}$$

where ρ represents the density, U_∞ the free-stream velocity, h is the step height, and μ is the dynamic viscosity of the fluid, and R denotes the gas constant.

The BFS is an interesting configuration due to the prevalence of flow separation and reattachment. Numerous investigations have been performed to comprehend the phenomenon of flow separation and reattachment over BFS. The studies regarding the effect of aspect ratio, Prandtl number, Reynold's number, and step height have been documented using numerical and analytical methods for 3D and 2D flow to further our understanding of the BFS. In general, near-space corresponds to a region where its altitude ranges from 20 kilometers to 100 kilometers [16] and attracts greater focus in modern times because of the defense applications. Many researchers have documented numerous investigations involving both experimental and computational approaches involving flow over basic geometries. The studies carried out also include the BFS flow in the subsonic [19, 20], supersonic [21, 22] and hypersonic [23, 24] domains, though most of them are in the continuum regime. Therefore, a few significant studies are discussed in this introduction.

Choi et al. [9] implemented a compressible Navier-Stokes Fourier (NSF) equation with Langmuir slip boundary condition for the BFS flow and accurately predicted the flow physics. Hsieh [10] investigated the 3D microscale BFS flow using the DSMC method. The study was carried out by simplifying the 3D configuration to 2D, and they examined the flow separation, recirculation and reattachment. Beskok [11] devised a velocity-slip boundary condition and applied the same for the BFS flows. Similarly, Celik and Edis [12] formed the Finite element form of the Navier-Stokes equation and implemented it for the BFS flows. Rached and Daher [13] used the conventional control-volume approach with slip/jump boundary conditions to explore the BFS flow. They compared their results with analytical findings and found a good agreement with each other. An analogous procedure for BFS was implemented by Baysal et al. [14]. Xue and Chen [15] used the DSMC method for flow past BFS on a microscale and investigated the rarefaction effects. Their outcomes indicated that the flow phenomena such as flow separation, reattachment and recirculation disappeared when Kn exceeded 0.1. Xue et al. [15] explained the reasons for the above phenomena in another study.

Nabapure and Kalluri [16] investigated the compressibility and effect of wall temperature on the hypersonic BFS flow using the DSMC method. Kursun and Kapat [17] used the DSMC-IP (Information preservation) method to investigate BFS flows. They carried out the studies for Re of 0.03 to 0.64, M of 0.013 to 0.083. For the above conditions, they did not report any recirculation region. Bao and Lin [18] studied the microscale-BFS flows using the continuum-based Burnett equations. They correlated their numerical findings with the available experimental and numerical results from the literature, which showed good agreement. Darbandi and Roohi [19] employed the DSMC technique to investigate the micro/nano-BFS flows in the subsonic domain and investigated the effect of rarefaction. Their results

https://doi.org/10.1017/aer.2021.88 Published online by Cambridge University Press

indicated a decrease in the separation region length as the flow entered the transitional regime. Mahadavi and Roohi [20] analysed the effects of rarefaction, pressure ratio and wall temperature for nano BFS flow using DSMC and studied the flow behaviour. Mahadavi et al. [21] analysed the micro/nano BFS by incorporating hybrid slip/jump boundary conditions in the NSF equations and evaluated the influence of various pressure ratios, inlet temperatures and wall temperatures. The results of their modified boundary condition predicted better compared to DSMC. Gavasane et al. [22] also used the DSMC method and analysed the rarefaction and pressure ratio effects on the micro-BFS with Argon as the fluid. Guo et al. [23] employed the DSMC method to investigate the BFS flow in the slip and transitional flow regime and explored the various flow characteristics. Leite et al. [6] used the DSMC technique to analyse the hypersonic BFS flow with non-reacting air as the fluid and inspected the aerodynamic properties for different step heights.

Also, various works have investigated the flow over cavities. Palharini et al. [3] used the DSMC method to study the impact of three-dimensionality on the aerodynamic characteristics of the cavity flow. Santos et al. [24] used the DSMC technique to investigate the effect of changing cavity height on the aerodynamic characteristics of a hypersonic cavity flow. Guo et al. [1] used the DSMC method to study rarefied flow across different cavity shapes and studied the flow field characteristics. In another study, Guo et al. [25] examined the flow-field properties of a 2D hypersonic cavity flow for different Knudsen numbers within the transitional regime. In similar research, Palharini et al. [26] used the DSMC technique to investigate the impact of changing cavity length for various (L/D) (length to depth) ratios in the cavity in the transitional regime. Jin et al. [27] used the DSMC method to investigate the effect of the Maxwellian accommodation coefficient on rarefied hypersonic flows across 3D cavity flows in the transitional regime.

Based on the above review, significant research exists on the rarefied flow over a BFS in different flow regimes. Nonetheless, the aerothermodynamic conditions encountered by hypersonic re-entry vehicles are challenging to analyse owing to the various complexities involved, which are not adequately recorded in the open literature. Most of the past research primarily concentrated on investigating the rarefaction effects at lower Knudsen numbers. Moreover, only a handful of studies have analysed the range of rarefaction regimes that the hypersonic re-entry vehicles encounter, but they are limited to the transitional flow regime. However, the re-entry vehicles typically experience higher levels of rarefaction at higher altitudes, and the rarefaction levels reduce as they descend back to the earth. However, to the best of the authors' knowledge, none of the previous investigations provide a comprehensive analysis of the effects of rarefaction on the flow and surface properties that a re-entry vehicle typically encounters during its flight, particularly in the free molecular regime. Thus, this paper aims to bridge the gap and explores the flow-field and aerodynamic properties for a range of Knudsen numbers covering different flow regimes from the slip to free-molecular.

Therefore, in the present analysis, we use the DSMC approach by adopting an open-source solver named *dsmcFoam* to analyse the rarefaction effects for flow over a BFS. The research objectives are to (i) to examine the rarefaction effects by considering a range of Knudsen numbers covering the slip to free-molecular regimes, (ii) to study the variation of the flow and surface properties at various locations along the transverse direction, (iii) to examine the recirculation regions formed and estimate the recirculation lengths for the different regimes (iv) to compare the non-reacting flows against the reacting flows and outline the differences.

2.0 Numerical methodology

In this section, the computational domain, a brief description of the computational approach employed for the analysis, and the various computational parameters used in the investigation are provided.

2.1 DSMC

Bird [28] introduced the direct simulation Monte Carlo (DSMC) technique in the mid-1960s, which is regarded as one of the most robust approaches for solving the Boltzmann equation. The DSMC

https://doi.org/10.1017/aer.2021.88 Published online by Cambridge University Press

solution is a useful computational method for simulating rarefied gas flows, whether reactive or not. This approach guides molecules into stages of decoupling, motion, and collision, using the kinetic theory to obtain non-continuum gas characteristics accurately. The DSMC is mainly used in simulating high-speed rarefied gas flows having higher levels of rarefaction.

As known, the air density declines steadily as the elevation rises, and the rarefaction effects influence the flow properties. Also, there is a breakdown of NSF equations [8], paving the way for the usage of the Boltzmann equation given as [29]:

$$\frac{\partial f}{\partial t} + v.\nabla_x f = \frac{1}{Kn} Q\,(f,f),\ x \in \mathbb{R}^{dx},\ v \in \mathbb{R}^{dv} \tag{3}$$

where $f(t, x, v)$ denotes the density distribution function of a dilute gas at a position x, velocity v and at time t. Kn represents the Knudsen number of the flow and the collision operator $Q\,(f,f)$ denotes the binary collisions taking place.

The basic rules of the DSMC approach comprise four main aspects: moving, indexing, collision and sampling. The DSMC scheme employs a mathematical framework that models the actual gas dynamics by the movement of various simulated particles represented as a conglomeration of several actual particles and determines their interactions. A parallel DSMC package is used in the current analysis to save computing power by utilising 32 cores. The computational domain comprising a structured 2D grid is split into cells for choosing the collision pairs. There are many schemes to select a collision pair; a review is given in Refs [30, 31]. Here the No Time Counter scheme(NTC) [32] is selected. Also, DSMC has a variety of collision models, which are explained in Ref. (33). The current study handles the intermolecular collisions using the Variable Hard Sphere (VHS) collision model.

The DSMC approach primarily depends on the proper selection of the cell size, particles per cell, and time step for generating accurate results. The cell size is usually chosen to be smaller than a third of the mean free path [34], and similarly, the time step is smaller than a third of the collision's mean time [35]. The above criteria are adapted in the present study. The particles per cell were 25 providing sufficient accuracy.

In this study, DSMC computations employed the open-source *dsmcFoam* code [36, 37]. The code is highly efficient and scalable by adapting efficient parallelisation techniques such as OpenMPI. Moreover, the code has been validated on various problems in rarefied gas flows.

2.2 Geometry and computational domain

The rarefied flow over a 2D BFS, as shown in Fig. 1, is the geometry considered for analysis. The study is conducted for a range of Knudsen numbers where the flow moves from left to right. X and Y denote the cartesian coordinates along the streamwise and transverse directions. The upstream length was kept at 60mm, including an initial 15mm length of the symmetry region. The downstream length considered was 105mm, and the step was located at 60mm from the inlet and is far enough from both the inlet and outlet. For all simulations, the step height (h) was set at 3mm. The channel height at the outlet was fixed at H = 60mm after conducting a domain independence study such that the top surface does not influence the flow-field and surface properties. The range of Kn studied was 0.05, 0.1, 1.06, 10.33, 21.10, covering all the rarefaction regimes.

2.3 Boundary conditions and mesh

The different boundary conditions applied on the surfaces are, as shown in the computational domain in Fig. 1. The left, top, and right boundaries represent the far-field boundary condition through which the simulated particles easily enter and leave the domain. The solid boundary (blue) represents the BFS and is given a diffused reflection with full thermal accommodation condition. In a diffuse reflection model, the simulated molecules are equally reflected in all directions. The initial length of 15mm from the inlet

https://doi.org/10.1017/aer.2021.88 Published online by Cambridge University Press

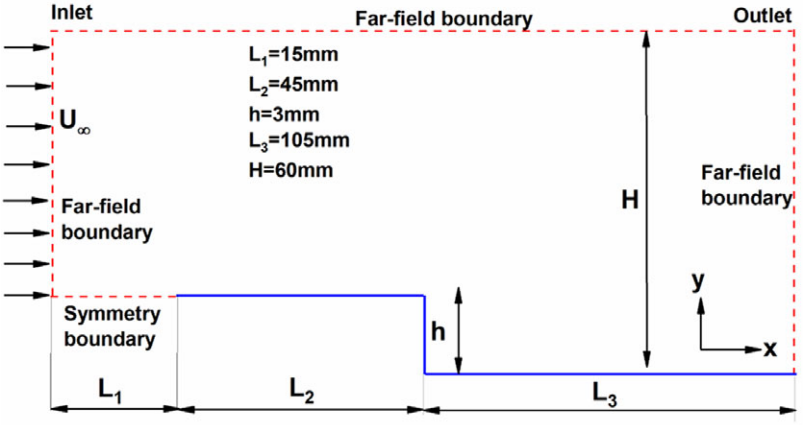

Figure 1. *Schematic of the 2D BFS.*

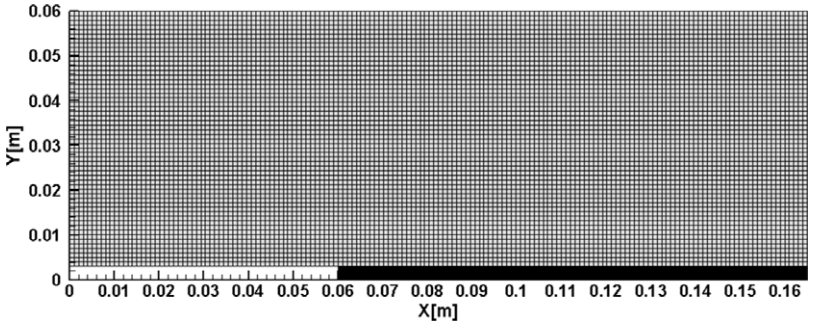

Figure 2. *Meshed domain.*

to the edge of the flat plate represents symmetry and is used to accomplish a precise velocity in the perpendicular directions [30]. Thus, this surface is analogous to a specular reflecting model.

The computational domain is divided into several blocks and meshed in a structured manner, as shown in Fig. 2. The cell widths in both X and Y directions were maintained below the mean free path, i.e. Δx_{cell}, $\Delta y_{cell} < 0.3\ \lambda_\infty$. The total number of cells for the case of $Kn = 1.06$ was about 11,250 cells. Also, the cell count varied for other cases depending on the corresponding mean free path.

Tables 1 and 2 show the gas properties and the free-stream flow parameters employed in the present simulations. Such flow characteristics are experienced by a hypersonic vehicle during its re-entry and are taken from the U.S. Standard Atmosphere charts [38]. In the initial studies, the fluid considered was non-reacting air, and the chemical reactions were relaxed. This assumption has been used in numerous published studies [3, 26, 27, 39]. Also, the fluid was assumed to have a molecular weight of about 28.96 g/mol with a major composition of 76% N_2 and 23% O_2. The inflow free stream M was set as 25 and was constant for all cases. The literature has various studies where the Mach number of 25 was considered [26, 39]. Also, since these vehicles travel at speeds greater than Mach 25, the downstream body surface still experiences velocities around Mach 25. Alternatively, the flow can be impinging at an angle in which case the flow directly encounters the BFS. Sharp or slender objects are other instances with a weak bow shock, which could result in the situation that is considered in the present study. All the wall surfaces (T_w) were maintained at four times the free-stream temperature $4T_\infty$.

In Table 1, χ denotes the mole fraction, m denotes the molecular mass, d the molecular diameter, ω represents the temperature dependent viscosity index, and ζ represents the degrees of freedom.

https://doi.org/10.1017/aer.2021.88 Published online by Cambridge University Press

Table 1. *Gas properties [39]*

	χ	ω	m, kg	ζ	d, m
O_2	0.237	0.77	5.312×10^{-26}	5	4.07×10−10
N_2	0.763	0.74	4.650×10^{-26}	5	4.17×10−10

Table 2. *Flow and simulation parameters [38]*

Altitude	55.02Km	60.5Km	77Km	91.5Km	95Km
Free-stream velocity (U_∞) [m/s]	8,050.75	7,829.25	7,134.5	6,851.38	6,887.03
Inlet gas temperature, (T_∞)[K]	259.39	245.64	204.49	186.89	188.84
Wall temperature, (T_w)[K]	1,037.56	982.56	817.96	747.56	755.36
Free-stream pressure, (p_∞)[N/m^2]	39.86	20.51	1.72	0.14	0.069
Mass density, (ρ) [kg/m^3]	5.35×10^{-4}	2.90×10^{-4}	2.94×10^{-5}	2.61×10^{-6}	1.27×10^{-6}
Mean free path, (λ_∞) [m]	1.51×10^{-4}	3×10^{-4}	3.19×10^{-3}	3.1×10^{-2}	6.33×10^{-2}
Number density, (n_∞)[per m^3]	1.11×10^{22}	5.62×10^{21}	5.29×10^{20}	5.45×10^{19}	2.66×10^{19}
Reynolds number (Re_h)	783.11	431.10	46.61	4.29	2.08
Knudsen number (Kn_h)	0.05	0.10	1.06	10.33	21.10

Table 2 lists the flow and simulation parameters, which show the different atmospheric altitudes examined, ranging from 55Km to 95Km. All the simulations ran for about 1.5ms, which consisted of 75,000 timesteps and employed about 276,500 simulated particles. The time averaging of the DSMC particle fields was started once the total DSMC particles reached a steady state. The solution was considered steady-state when the average linear kinetic energy of the system showed no significant variation [36]. The Knudsen number (Kn_h) and Reynolds number (Re_h) were estimated by choosing the step height (h) as the characteristic dimension.

In the later part of the study, the comparison of chemically reacting flows with non-reacting flows was carried out. This section briefly describes the details of the chemical modeling. Several chemical reaction models, like the Total Collision Energy (TCE) model, introduced by Bird [40], are available in the DSMC. Predominantly the popular TCE utilises the equilibrium kinetic theory to correlate the macroscopic and microscopic properties of the gas by translating the Arrhenius rate coefficients into collision probabilities, which are a function of macroscopic gas temperature and microscopic collision energy, respectively. In recent years, an alternative reaction model, the Quantum-Kinetic (Q-K) chemistry model, was proposed by Bird [41]. This model is used in the present study and has been employed in *dsmcFoam+* code.

The Q-K method is a molecular level chemistry model that employs the fundamental molecular properties, antithetical to the classical TCE model, which relies on experimental data availability. In this study, the Q-K chemistry model has been used to define the chemical reactions of a five-species air model with a total of 19 chemical reactions in the *dsmcFoam+*. Two chemical reaction types are relevant to the present discussion: Dissociation (No. 1–15 in Table 3) and Exchange reactions (No. 16–19 in Table 3).

The overall temperature is defined as the weighted average of translational, rotational, and vibrational temperatures [42] and is given by,

$$T_{ov} = \frac{3T_T + \xi_R T_R + \xi_V T_V}{3 + \xi_R + \xi_V} \tag{4}$$

https://doi.org/10.1017/aer.2021.88 Published online by Cambridge University Press

Table 3. *List of chemical reactions employed*

No.	Reaction	Heat of formation $\times 10^{19}$ J
1	$O_2 + N \rightarrow O + O + N$	8.197
2	$O_2 + NO \rightarrow O + O + NO$	8.197
3	$O_2 + N_2 \rightarrow O + O + N_2$	8.197
4	$O_2 + O_2 \rightarrow O + O + O_2$	8.197
5	$O_2 + O \rightarrow O + O + O$	8.197
6	$N_2 + O \rightarrow N + N + O$	15.67
7	$N_2 + O_2 \rightarrow N + N + O_2$	15.67
8	$N_2 + NO \rightarrow N + N + NO$	15.67
9	$N_2 + N_2 \rightarrow N + N + N_2$	15.67
10	$N_2 + N \rightarrow N + N + N$	15.67
11	$NO + N_2 \rightarrow N + O + N_2$	10.43
12	$NO + O_2 \rightarrow N + O + O_2$	10.43
13	$NO + NO \rightarrow N + O + NO$	10.43
14	$NO + O \rightarrow N + O + O$	10.43
15	$NO + N \rightarrow N + O + N$	10.43
16	$NO + O \rightarrow O_2 + N$	2.719
17	$N_2 + O \rightarrow NO + N$	5.175
18	$O_2 + N \rightarrow NO + O$	−2.719
19	$NO + N \rightarrow N_2 + O$	−5.175

where ξ is the degree of freedom and the subscripts T, R and V stand for translation, rotation and vibration, respectively.

The following equations give the translational, rotational and vibrational temperatures,

$$T_T = \frac{1}{3k_b} \frac{\sum_{j=1}^{N} m_j c'^2}{N} \tag{5}$$

$$T_R = \frac{2}{k_b \xi_R} \frac{\sum_{j=1}^{N} (\varepsilon_R)_j}{N} \tag{6}$$

$$T_V = \frac{\Theta_V}{\ln\left(1 + \frac{k_b \Theta_V}{\sum_{j=1}^{N} (\varepsilon_V)_j}\right)} \tag{7}$$

where k_b is the Boltzmann constant, ε_R and ε_V represent the average rotational and vibrational energies and Θ_V denotes the characteristic vibrational temperature, which has a value of 3,371K and 2,256K for N_2 and O_2 respectively. The rotational and vibrational collision relaxation number considered in the study was 5 and 50, respectively.

3.0 Model validation and verification

In the section, the validation studies performed to assess the accuracy of the solver are explained. Without considering the chemical reactions, the validation was performed for a comparable case of flow over a BFS. Furthermore, the solver was validated, accounting for the chemical reactions using a cylinder test case. Also, the verification studies carried out to predict the results accurately are presented.

https://doi.org/10.1017/aer.2021.88 Published online by Cambridge University Press

Table 4. *Computational details of Guo et al. [23]*

H	P_0	T_0	M_∞	Step height	Mean free path	Collision frequency	Inflow density
(Km)	(Pa)	(K)	–	(mm)	(m)	(1/s)	(kg/m^3)
30	1,197	226.5	6	10	4.41×10^{-6}	9.22×10^{7}	$\times 10^{-2}$ 1.50

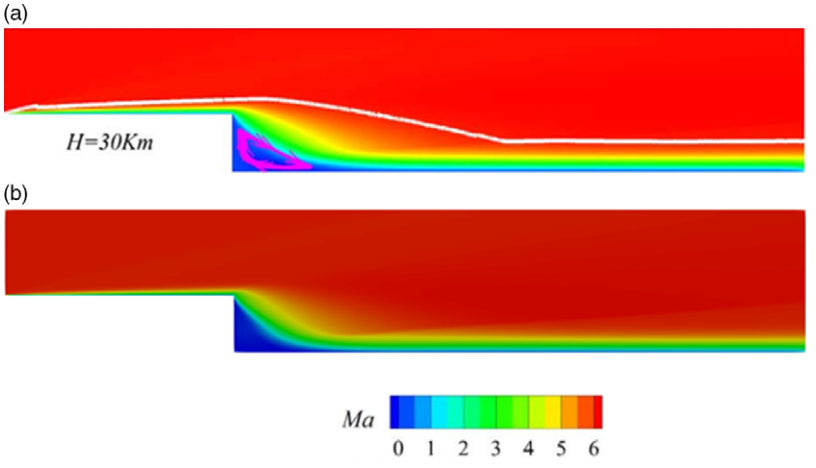

Figure 3. *Comparison of velocity contour for the case of $H = 30$Km (a) published results [23] (b) simulation results.*

3.1 Validation

3.1.1 Flow over BFS

In the present study, the investigations are performed by utilising the *dsmcFoam* solver. The solver has been validated for different cases [43–51]. For the comparable case of flow over BFS, the results predicted by the current model using the DSMC method are compared with the numerical results of Guo et al. [23]. Guo et al. [23] investigated the flow characteristics of a hypersonic BFS of step height 10mm in the slip and transitional regime using the DSMC method. The simulation parameters adopted for the case of H = 30Km are shown in Table 4. For visual validation, the velocity contours reported by Guo et al. were compared and are presented in Fig. 3, which shows a good agreement.

Additionally, the streamwise velocity and the pressure normal to the BFS surface at $X/h = 5$ are shown in Fig. 4. Where X represents the axial distance normalised by the free-stream step height (h). From the streamwise velocity profile, it is observed that both the results show reasonable agreement, with a slight discrepancy near the wall. Also, the comparison of the pressure shows a fair match between our results with the published results. Thus, our findings match well with Guo et al., thus validating the current study's numerical model.

3.1.2 Chemically reacting flow over a circular cylinder

To validate the solver incorporating the chemical reactions, a test case of the cylinder was simulated. A two-dimensional hypersonic rarefied air flow over a circular cylinder with a diameter of 2m, investigated by Scanlon et al. [52], was used as a benchmark case, and the Quantum-Kinetics (Q–K) chemical reaction model was considered. The free-stream and flow conditions for atmospheric altitude, $H = 86$Km, are shown in Table 5. Figure 5(a) compares Mach number contours reported by Scanlon et al. and the present simulation. Figure 5(b) depicts the species' number density along the stagnation line in front of the cylinder. The results obtained match well with the Q–K results of Scanlon et al., thus, supporting the validity of our results for chemically reacting rarefied flow in the present work.

https://doi.org/10.1017/aer.2021.88 Published online by Cambridge University Press

Table 5. *Computational details of Scanlon et al. [52]*

H	T_∞	Ma_∞	Cylinder diameter	Mean free path	Collision frequency	Inflow density
(Km)	(K)	–	(m)	(m)	(1/s)	(kg/m^3)
86	187	25	2	1.23×10^{-2}	2.96×10^4	$\times 10^{-5}$ 1.43

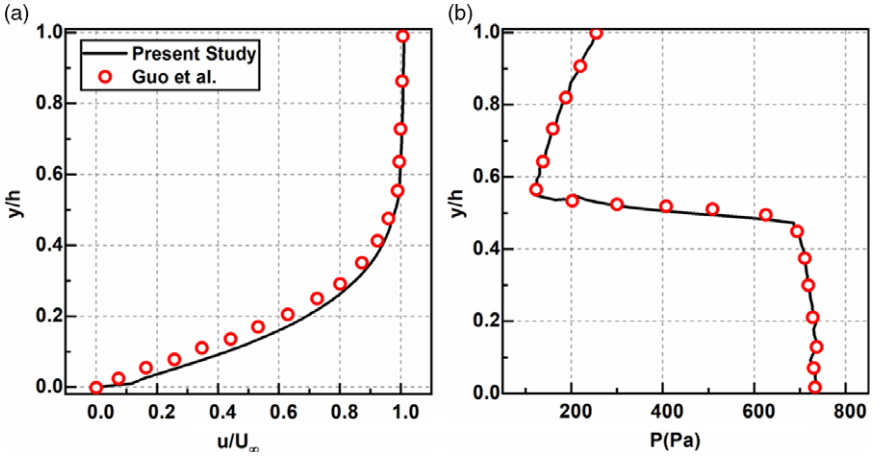

Figure 4. *Comparison of (a) streamwise velocity and (b) pressure along the vertical line of $X/h = 5$ for the case of $H = 30$Km.*

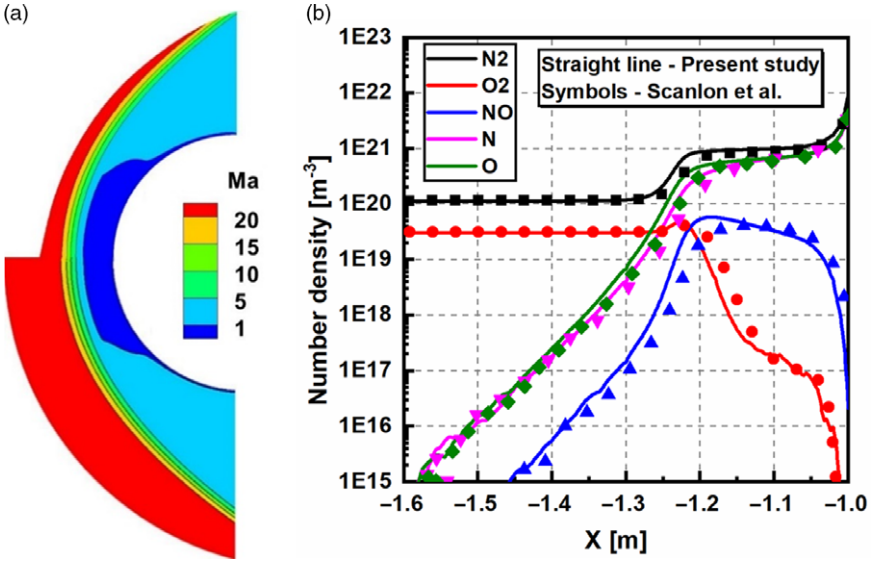

Figure 5. *(a) Comparison of overall Mach number contour between published Q–K results by Scanlon et al. [52] (lower half) and present simulation results (upper half), (b) Comparison of number density along the stagnation line.*

3.2 Verification

The various errors involved in the DSMC technique [53] are thoroughly examined in the present section. The verification studies are typically carried out for cell size, time-step, particles per cell, and number of

https://doi.org/10.1017/aer.2021.88 Published online by Cambridge University Press

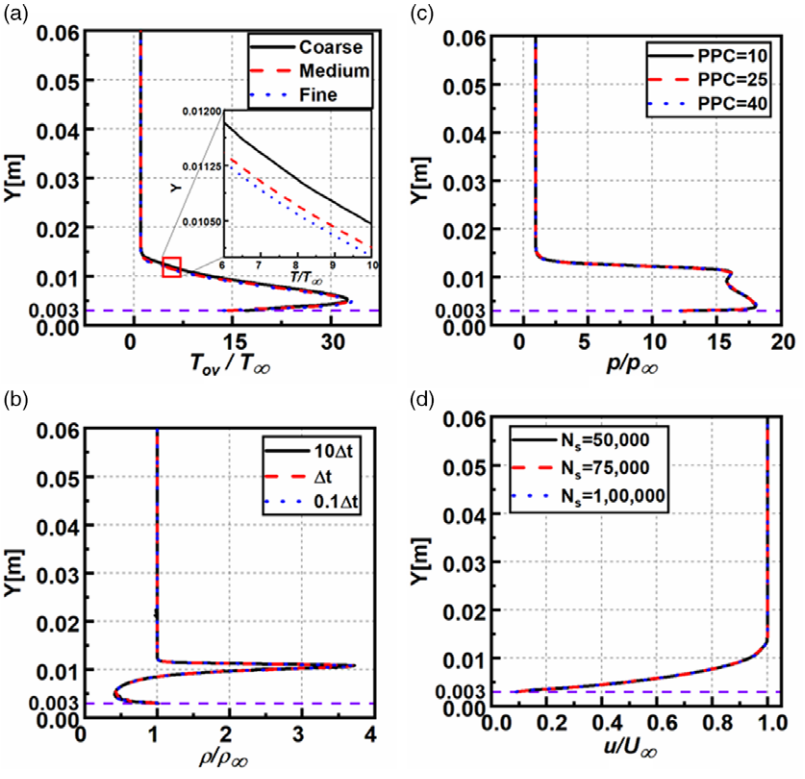

Figure 6. *Variation of the non-dimensional (a) overall temperature, (b) density, (c) velocity and (d) pressure in the transverse direction of BFS at* $X = 120$mm *for* $H = 60$mm, $Kn = 0.05$.

samples [23, 39]. For grid independency, the flow past BFS for $M = 25$, $Kn = 0.05$, and $H = 60$mm were investigated for different grids, namely, coarse, medium, and fine. The coarse grid consisted of 50% less cells than the medium grid, whereas the fine grid had 50% additional cells. Furthermore, cell ratio (Δx) to mean free path (λ) considered was 0.3. Figure 6(a) shows the non-dimensional overall temperature at $X = 59$mm for the grids considered. (The dashed purple line in the figures represent the level of the step height $h = 0.003$m. The profile shows a close match for the medium and fine grids. Thus, to reduce the computational time, the medium grid (shown in Fig. 2) was used in all the simulations. Also, the grid was changed as per the mean free path of the corresponding Knudsen number case.

Likewise, for three distinct timesteps, i.e. 10 Δt, Δt, and 0.1 Δt, a time-independence evaluation was carried out, with $\Delta t = 2 \times 10^{-8}$s. For the timesteps considered, the ratio of the time step to the mean collision time are $\Delta t/\Delta t_{mc} = 1.17 \times 10^{-3}$, 1.17×10^{-4}, 1.17×10^{-4}, respectively. As a result, all the timesteps assumed were smaller than the mean collision time. Figure 6(b) represents the non-dimensional density for the timesteps, which show a close match for Δt and 0.1 Δt. This suggests that the selected standard time step is sufficiently small to ensure that computational findings are timestep independent. Thus, a $\Delta t = 2 \times 10^{-8}$s was adopted.

Also, to select an optimum particle per cell (PPC), simulations were performed for three distinct PPC, namely 10, 25, and 40. Figure 6(c) shows the non-dimensional pressure at $X = 59$mm for the three PPC's considered, showing an overlapping trend for PPC of 25, 40. Hence a PPC of 25 was adopted.

A final study was carried out to choose the total number of samples (N_s) required. Figure 6(d) shows the non-dimensional velocity at $X = 59$mm, which overlaps for $N_s = 75{,}000$ and $N_s = 1{,}00{,}000$. Thus $N_s = 75{,}000$ was selected. Therefore, the present study's computational model provides a reasonably good prediction of the cases investigated.

https://doi.org/10.1017/aer.2021.88 Published online by Cambridge University Press

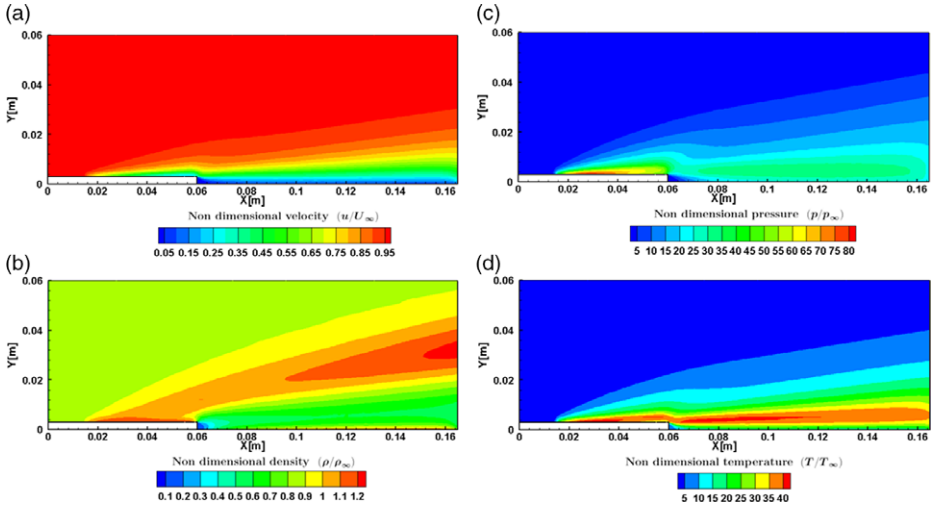

Figure 7. *Contours of non-dimensional (a) velocity, (b) density, (c) pressure and (d) overall temperature for* $H = 60$mm, $M = 25$ *and* $Kn = 1.06$.

4.0 Numerical results and discussion

In order to study the rarefaction effects on the flow past BFS, five distinct Knudsen numbers (given in Table 2) in various rarefaction regimes are simulated, and the flow field and surface characteristics are analysed. For all the instances, the free-stream Mach number considered was 25, with a step height of ($h = 3$mm), and the wall surface (T_w) was maintained at four times the free-stream temperature $4T_\infty$. The various flow features are evaluated vertically at four different X locations, namely $X = 30$, 59, 61, and 120mm, respectively.

4.1 Flow-field properties

4.1.1 Flow contours

For the case of $M = 25$, $Kn = 1.06$, and $H = 60$mm, the various flow-field contours are shown in Fig. 7(a–d). Figure 7(a) shows the non-dimensional velocity contour depicting the growth of hydrodynamic boundary layer, with lower magnitudes at the wall and higher magnitudes away from it in the central domain. Downstream of the step due to the recirculation region's formation, the velocity magnitudes are very low. Also, the band of near-wall low velocity extends from the step to the outlet region.

The non-dimensional density contour shown in Fig. 7(b) shows a higher density near the upstream wall and a gradual reduction away from it. The density magnitude is close to one in most of the computational domain. The region close to the step has low density magnitudes due to the recirculation and expansion effects. Furthermore, a high-density magnitude band arises from the upstream surface and traverses towards the top surface, causing a regionalised density rise.

The non-dimensional pressure contour is shown in Fig. 7(c), which attain greater values at the upstream wall and are one order greater than that of the free stream. Due to the minimal influence of the step in the central domain, pressure attains the free-stream value. In the downstream direction, the pressure magnitudes are very low due to the recirculation. Also, the wall pressures are lower than their upstream counterparts, primarily due to the flow expansion.

The non-dimensional overall temperature contour is shown in Fig. 7(d), which follows the pressure contour and depicts higher magnitudes near the wall due to the viscous heating and compressibility phenomena. The band of high temperature at the step height level continues to dissipate the energy

https://doi.org/10.1017/aer.2021.88 Published online by Cambridge University Press

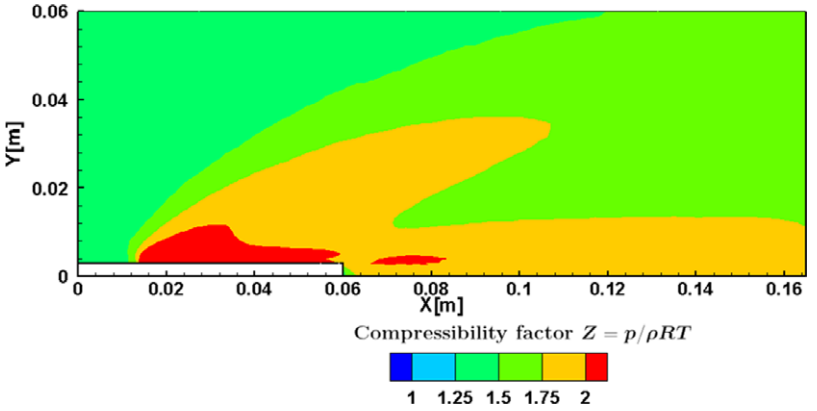

Figure 8. *Compressibility (Z) contour for* $H = 60$mm, $M = 25$ *and* $Kn = 1.06$.

farther downstream of the step. Like the pressure contour, the non-dimensional temperature also shows lower magnitudes close to the step; however, these low temperatures are confined to a lower region than the pressure.

The Compressibility (Z) contour is shown in Fig. 8. The compressibility factor shows the departure of the gas from the ideal behaviour and is given by

$$Z = \frac{p}{\rho RT} \tag{8}$$

where p denotes the pressure, ρ the density, R the gas constant, and T is the temperature.

The regions of higher Z magnitudes are witnessed on the upstream surface due to the shear effects. A similar trend is noticed downstream of the step; however, the magnitudes of Z are lower compared to the upstream. In the region close to the step and the center of the domain, the magnitudes of Z are relatively low, depicting equilibrium.

4.1.2 Velocity field

The non-dimensional velocity (u/U_∞) distribution for various Kn at sections $X = 30$mm, $X = 59$mm, $X = 61$mm, and $X = 120$mm is depicted in Fig. 9(a-d). Y represents the perpendicular distance in y-direction above the BFS surface.

The profiles at section $X = 30$mm and $X = 59$mm are similar, depicting the flow is undisturbed upstream of the step. At Section $X = 61$mm, the velocity profiles show negative magnitudes, portraying recirculation; a similar phenomenon was found in Grotowsky and Ballmann's [54] continuum regime analysis. Interestingly, at section $X = 61$mm up to the step height, the (u/U_∞) profiles overlap for all regimes and show a diverging trend above the step. The profiles close to the outlet at $X = 120$mm remain relatively unaffected, like those at the inlet. However, the velocity slip at the wall is significant for all sections, excluding section $X = 61$mm, where the slip is relatively the same for all the regimes [55]. This trend deviates from the traditional continuum results, which show zero velocity at the walls.

The rarefaction effects also reduce the non-dimensional velocity along Y. The increase in rarefaction reduces the intermolecular collisions and increases the molecular mean free path. Consequently, the wall effects propagate more into the flow field, reducing the velocity. This is quantified by the boundary layer thickness, another important flow characteristic. Here, the boundary layer thickness (δ) is extracted considering the point where $u/U_\infty = 0.99$. For the top surface location considered in the present study, the boundary layer is fully established for different Kn, except $Kn = 21.10$, which shows a developing trend. For a particular location of $X = 59$mm, (δ) and (δ/H) are given in Table 6.

https://doi.org/10.1017/aer.2021.88 Published online by Cambridge University Press

Table 6. *Thickness of the boundary layer (δ) for various Kn at $X = 59$mm*

Kn	0.05	0.10	1.06	10.33	21.10
δ(mm)	8.3	9.65	26.7	55.4	–
δ/H	0.13	0.16	0.44	0.92	–

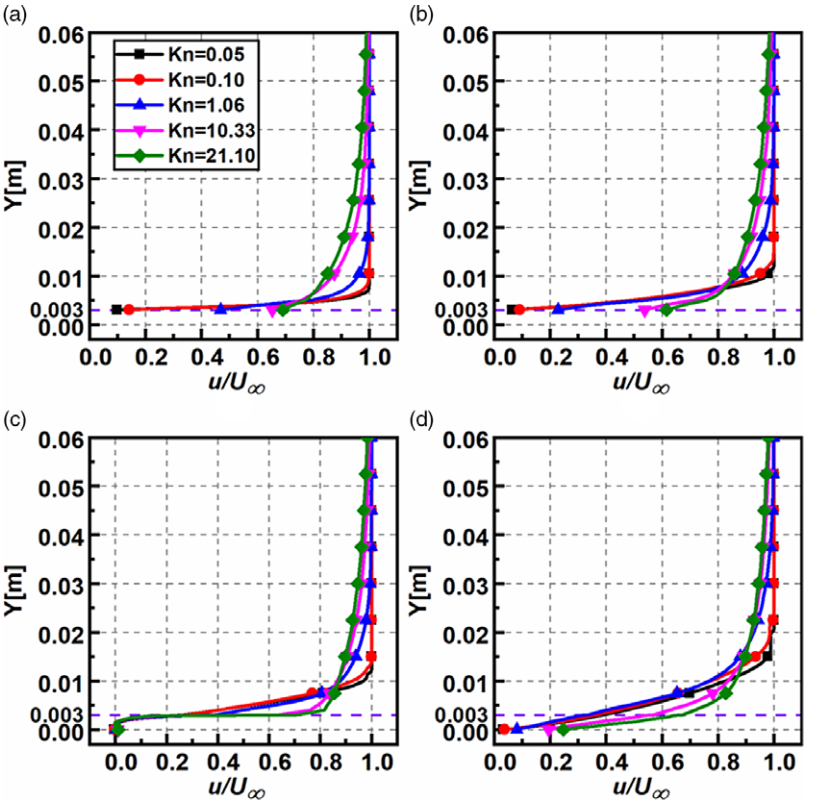

Figure 9. *Non-dimensional velocity variation for various Kn at (a) $X = 30$mm, (b) $X = 59$mm, (c) $X = 61$mm and (d) $X = 120$mm.*

The near-wall velocity (slip) also increases with rarefaction. The profiles for different rarefaction regimes at a given Y location also differ only slightly from each other. At section $X = 61$mm, magnitudes of (u/U_∞) at $Y = 0.03$ are 1.00, 0.99, 0.99, 0.96 and 0.94 for *Kn* 0.05, 0.1, 1.06, 10.33 and 21.10, respectively.

The velocity streamlines for different *Kn* are depicted in Fig. 10. It is observed that for all *Kn*, a recirculation region exists. Furthermore, streamlines of the free-molecular flow for the case of $Kn = 21.10$ suggests that there exists a secondary smaller recirculation region. The lengths of recirculation for various *Kn* in is given in Table 7. These lengths are calculated from the corner of the step (i.e. from $X = 60$mm) and are denoted by $X_L$and Y_L. These are extracted where the skin friction coefficient $(C_f = 0)$ [56, 57]. Both X_L and Y_L show a diminishing value with *Kn* [15] (as Re decreases as seen from Table 2). This behaviour is analogous to the one found in continuum flows for decreasing Reynolds number.

https://doi.org/10.1017/aer.2021.88 Published online by Cambridge University Press

Table 7. *Recirculation lengths for different Kn*

Kn	0.05	0.1	1.06	10.33	21.10
$\mathbf{X}_L$**(mm)**	1.95	1.65	1.40	1.21	1.15
$\mathbf{Y}_L$**(mm)**	1.55	1.53	1.44	1.42	1.18

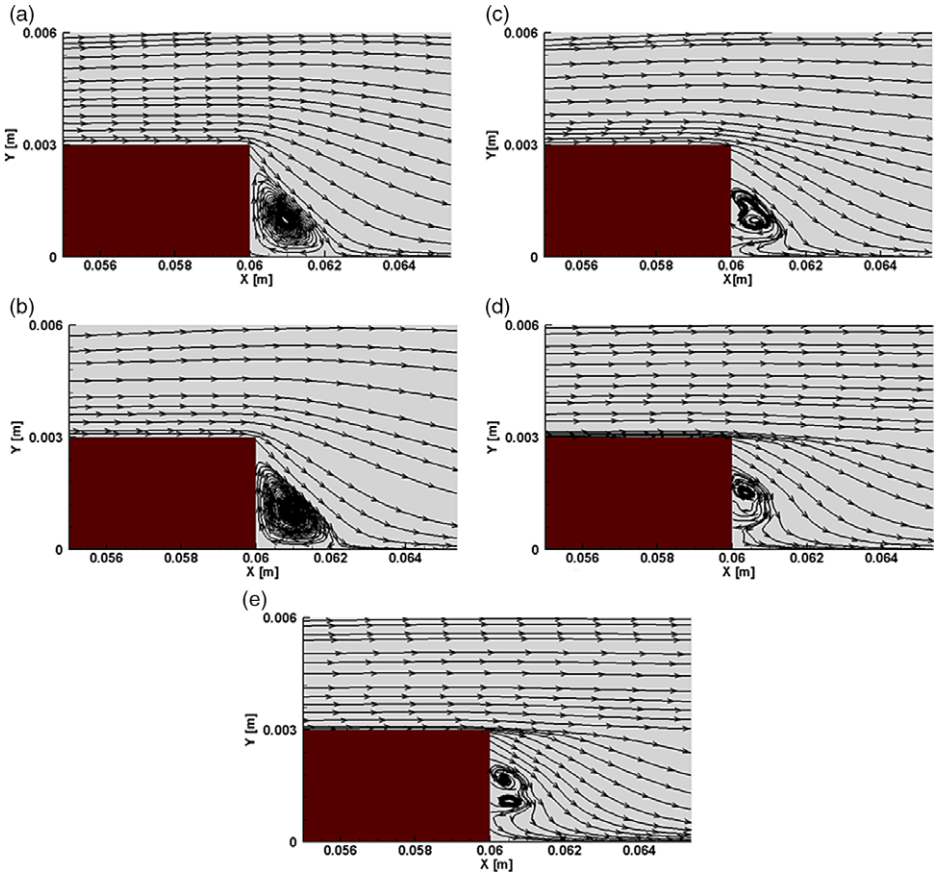

Figure 10. *Velocity streamlines for (a)* $Kn = 0.05$*, (b)* $Kn = 0.1$*, (c)* $Kn = 1.06$*, (d)* $Kn = 10.33$ *and (e)* $Kn = 21.10$*.*

4.1.3 Velocity slip

The plots of non-dimensional velocity slip (u_s/U_∞) for different *Kn* on the upper, lower surfaces is shown in Fig. 11. The slip is calculated considering the difference in wall velocity and the fluid close to the wall. It can be extracted by direct sampling of the microscopic particles impacting the wall. It can also be obtained by retrieving the macroscopic flow properties in the cell adjacent to the wall [58]; the latter is used in this analysis.

The velocity slip reduces non-linearly towards the step. Towards the upper surface's leading edge, the velocity difference between the incoming flow and the wall is large, which leads to a peak in the velocity slip. This decreases downstream as the presence of the wall decelerates the flow. The velocity slip increases along the lower surface downstream of the step, possibly because a larger part of the flow domain gains temperature.

https://doi.org/10.1017/aer.2021.88 Published online by Cambridge University Press

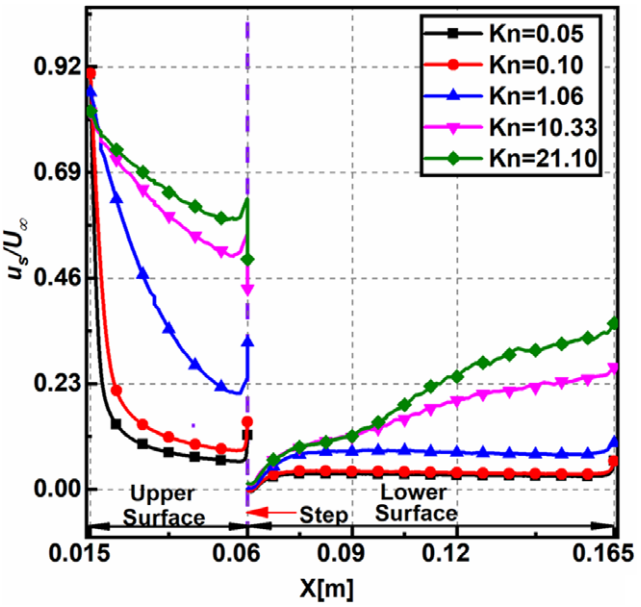

Figure 11. *Non-dimensional velocity slip on the upper and lower surfaces for various Kn.*

Upstream and downstream of the step, the velocity slip increases with *Kn* due to increased rarefaction effects. For lower *Kn*, the non-dimensional velocity slip at a given location is less and almost a constant compared to the other cases.

4.1.4 Pressure field

The non-dimensional pressure (p/p_∞) distribution for various *Kn* at sections $X = 30$mm, $X = 59$mm, $X = 61$mm, and $X = 120$mm is presented in Fig. 12(a–d). The non-dimensional pressure behaves similarly in all the sections and increases with increasing the Knudsen number. Also, close to the step, the pressure surpasses the free-stream values by an order of magnitude. There is a considerable variation in the near-wall pressure for different *Kn* at all the sections, except at $X = 61$mm, where it is approximately the same. Moreover, the pressure at a specified X attains the free-stream values quicker for $Kn = 0.05, 0.10$. In section $X = 61$mm, the pressure in the wake region of the step (for $Y < 0.003$) is close to the free-stream magnitude. Further away from the wall (for $Y > 0.003$), the pressure reaches a peak (owing to the presence of shock layer upstream) and gradually decreases to free-stream value. In $X = 120$mm, the pressure profiles behave like those at section $X = 61$mm, but with a marginally lower magnitude. At sections $X = 61$mm, $X = 120$mm, the pressure magnitudes decrease due to sudden expansion. Also, due to the compressibility effects of the free-stream flow, there is a pressure surge in all the plots near the step's face and is highest in the free-molecular regime. For evaluation, in section $X = 61$mm, the peak pressure ratios are 15.10, 16.01, 36.35, 48.94 and 42.80 for *Kn* 0.05, 0.1, 1.06, 10.33 and 21.10, respectively.

4.1.5 Temperature field

The non-dimensional overall temperature (T_{ov}/T_∞) variation for different *Kn* at sections $X = 30$mm, $X = 59$mm, $X = 61$mm and $X = 120$mm is described in Fig. 13(a–d). The magnitudes of T/T_∞ increases with *Kn* at all the sections. Moreover, there is a considerable variation in the near-wall temperature at all the sections, except at $X = 61$mm. Because of the substantial flow speed, the viscous heating rates result in a high magnitude of near-wall temperatures. In contrast, at $X = 61$mm, near the vicinity of the step, the temperature near the wall is nearly the same for different *Kn*.

https://doi.org/10.1017/aer.2021.88 Published online by Cambridge University Press

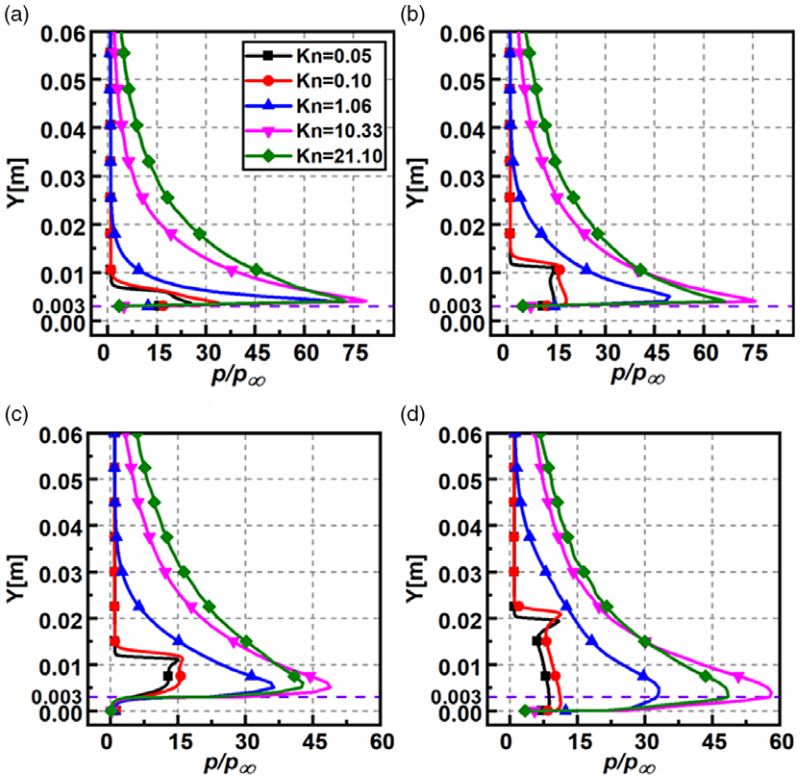

Figure 12. *Non-dimensional pressure variation for various Kn at (a)* $X = 30$mm*, (b)* $X = 59$mm*, (c)* $X = 61$mm*, and (d)* $X = 120$mm.

At the midpoint of the domain, at $Y = 0.03$, the non-dimensional temperature increases with *Kn*. As *Kn* increase, the molecules' number density reduces; thus, the viscous heating occurring in the shear layer is dissipated among lesser molecules causing higher magnitudes of non-dimensional temperature [59]. However, for smaller *Kn* in the slip and transitional regimes, the number density is several orders higher than the free-molecular regime. Thus, the same viscous heating levels are dispersed among more molecules, causing the overall temperature reduction. For quantitative assessment, at the section $X =$ 61mm, the non-dimensional temperature at $Y = 0.03$ are 0.99, 0.99, 2.31, 7.73 and 9.92 for *Kn* 0.05, 0.1, 1.06, 10.33 and 21.10, respectively.

In the transverse direction from the BFS surface, the non-dimensional temperature surges quickly decrease and reach values close to free-stream magnitudes. Again, for quantitative assessment at section $X = 61$mm, on the top face of the step, the peak temperature ratios are 29.38, 30.69, 37.65, 38.48 and 35.50 for *Kn* 0.05, 0.1, 1.06, 10.33 and 21.10, respectively. Thus, the non-dimensional temperature follows an identical pattern in all sections and reasonably shows an increasing trend with *Kn*.

Figure 14(a–d) shows the non-dimensional rotational (T_R), overall (T_{OV}), and translational temperature (T_T) in the perpendicular direction at sections $X = 30$mm, $X = 59$mm, $X = 61$mm and $X = 120$mm for $Kn = 0.05, 21.10$. The temperature profiles show a common trend in all sections. However, the magnitudes of the temperature in the free-molecular regime of $Kn = 21.10$ is greater than the slip regime of $Kn = 0.05$. This trend can again be attributed to the number density variation and the dispersion of the viscous heating effects among a lesser number of particles at high *Kn*, as explained earlier. The thermal boundary layer thickness grows as the flow traverses downstream, which can be seen in the peaks near the step height ($Y = 0.003$), which grows in size. The rotational temperature component shows appreciable variation only in the slip regime, demonstrating that at higher degrees of rarefaction, most of the energy

https://doi.org/10.1017/aer.2021.88 Published online by Cambridge University Press

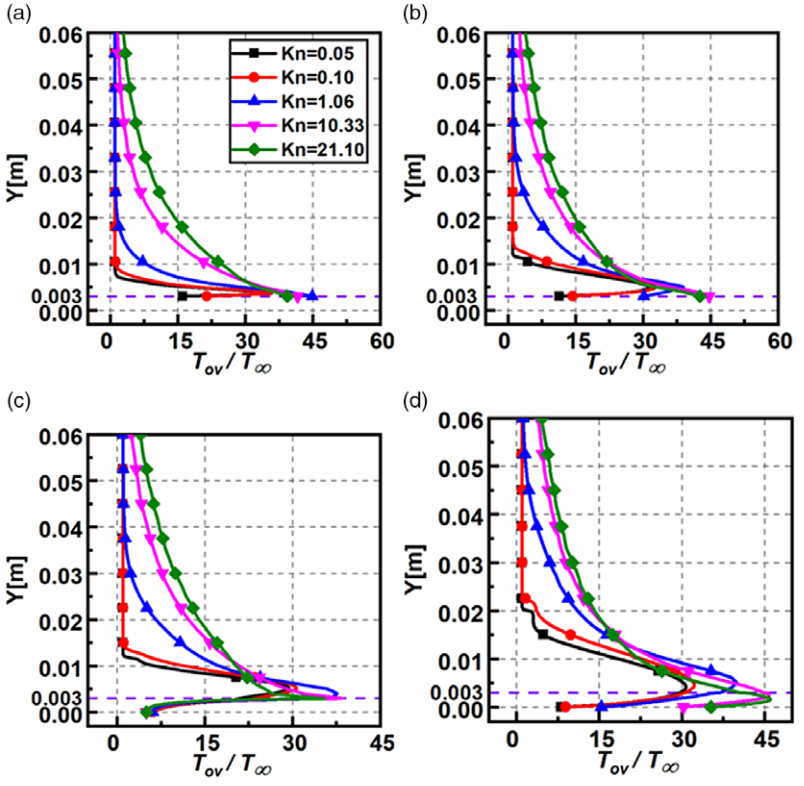

Figure 13. *Non-dimensional overall temperature variation for various Kn at (a)* $X = 30$mm*, (b)* $X = 59$mm*, (c)* $X = 61$mm*, and (d)* $X = 120$mm*.*

generated due to the wall and shear layer effects manifests itself in the translational and overall temperature components. Also, the change in the rotational component is noticed only at lower *Kn*, whereas at higher *Kn* the rotational component reasonably remains the same at all sections. Furthermore, the rotational component at the wall increases close to the outlet section of $X = 120$mm when compared to the wake of the step of $X = 61$mm.

4.1.6 Temperature jump

The plots of the non-dimensional temperature jump $\left(T_j/T_{\infty}\right)$ for different *Kn* on the upper, lower surfaces is shown in Fig. 15. The temperature jump is deduced similarly to the velocity slip. For a specified location, the temperature jump shows an increase with *Kn*. On the upstream surface for $Kn \leq 1.06$, the temperature jump reaches a peak and decreases towards the step, whereas it continually increases for $Kn \geq 10.33$. The wall temperature increase causes a surge in the near-wall fluid temperature, consequently increasing the local mean free path and the rarefaction. This increase in the rarefaction leads to an increase in the temperature jump. The wall shear rates soon decrease downstream of the leading edge and reduce the near-wall temperature and the resulting rarefaction effects. Moreover, the peak value of the temperature jump is about the same for different *Kn*. Additionally, on the lower surface, the temperature jump increases with *Kn* like the non-dimensional temperature.

4.1.7 Density field

The non-dimensional density (ρ/ρ_{∞}) variation for different *Kn* at sections $X = 30$mm, $X = 59$mm, $X = 61$mm and $X = 120$mm is shown in Fig. 16(a–d). The non-dimensional density varies significantly in

https://doi.org/10.1017/aer.2021.88 Published online by Cambridge University Press

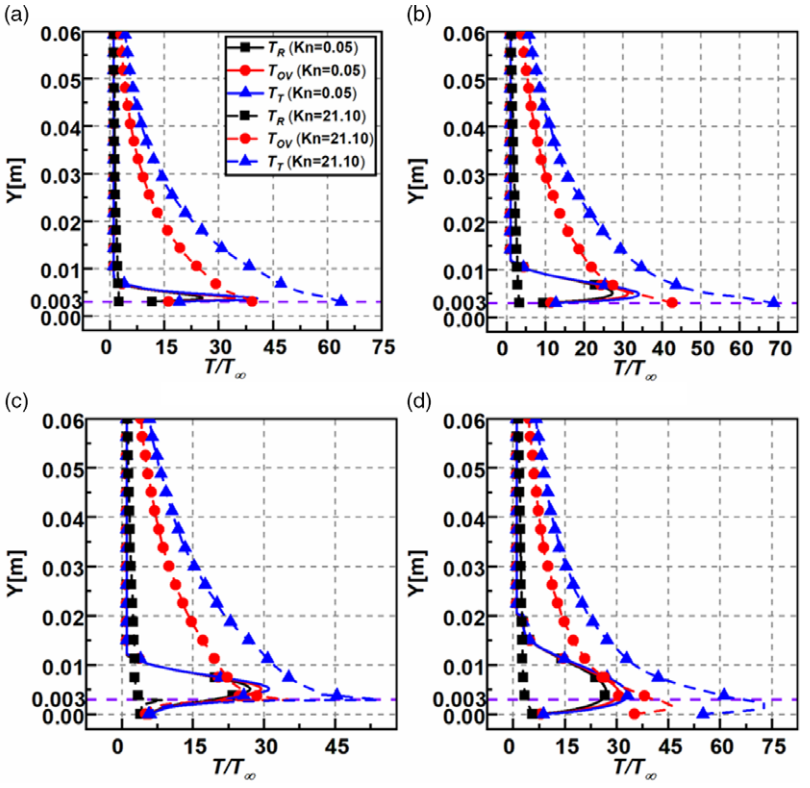

Figure 14. *Variation of the non-dimensional rotational, overall, and translational temperature for* $Kn = 0.05, 21.10$ *at (a)* $X = 30$mm*, (b)* $X = 59$mm*, (c)* $X = 61$mm *and (d)* $X = 120$mm*.*

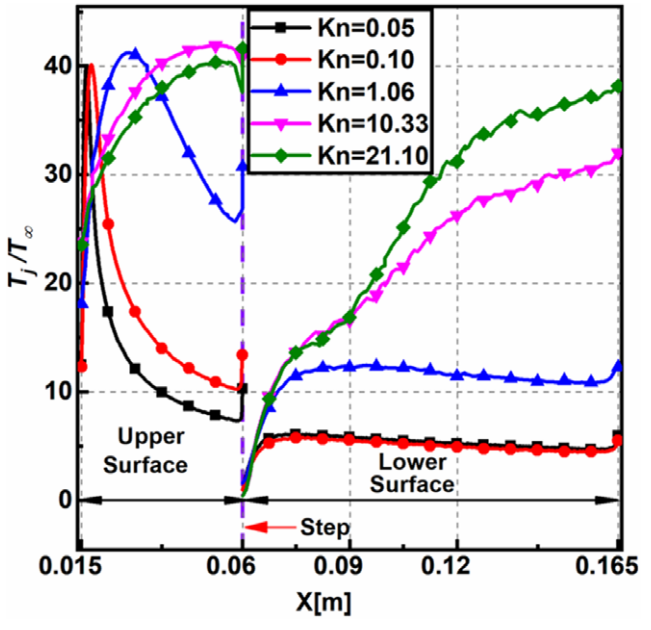

Figure 15. *Non-dimensional temperature jump on the upper and lower surfaces for various Kn.*

https://doi.org/10.1017/aer.2021.88 Published online by Cambridge University Press

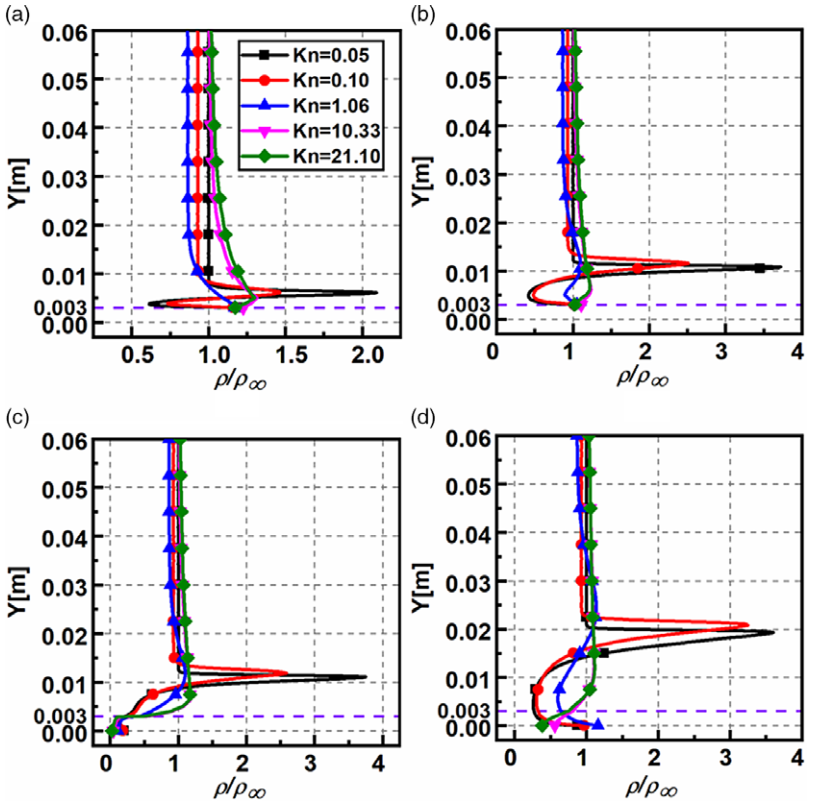

Figure 16. *Non-dimensional density variation for various Kn at (a)* $X = 30$mm*, (b)* $X = 59$mm*, (c)* $X = 61$mm *and (d)* $X = 120$mm*.*

the transverse direction, a common feature found in all sections. Another common feature is that the peak density in all sections is observed in the slip regime for $Kn = 0.05$ where it is about four times higher than the free-stream magnitude. At section $X = 30$mm, the non-dimensional density variation for different Kn at a given Y is noticeable, whereas, in other sections, it is not. At section $X = 61$mm, the densities at the wall are substantially smaller and almost overlap for different Kn. The densities for different Kn are relatively similar all along the face of the step and show a deviating trend after that, signifying that density variation is uninfluenced by a change in Kn in the recirculation region. Far away from the step ($Y > 0.003$),the density decreases beyond the shock wave and eventually tends to the free-stream density. At section $X = 120$mm, near the outlet, the density reduces up to $Y = 0.003$, then experiences a rise attributable to the shock region and, eventually, a reduction to attain the free-stream magnitude. For quantitative evaluation, in section $X = 61$mm, the peak density ratios are 3.751, 2.589, 1.100, 1.172 and 1.170 for Kn 0.05, 0.1, 1.06, 10.33 and 21.10, respectively.

4.2 Aerodynamic surface properties

4.2.1 Pressure coefficient

The pressure coefficient (C_p) distribution for various Kn on the upper and the lower surfaces of the BFS is shown in Fig. 17, C_p is given by

$$C_p = \frac{p_w - p_\infty}{\frac{1}{2}\rho_\infty U_\infty^2} \tag{9}$$

https://doi.org/10.1017/aer.2021.88 Published online by Cambridge University Press

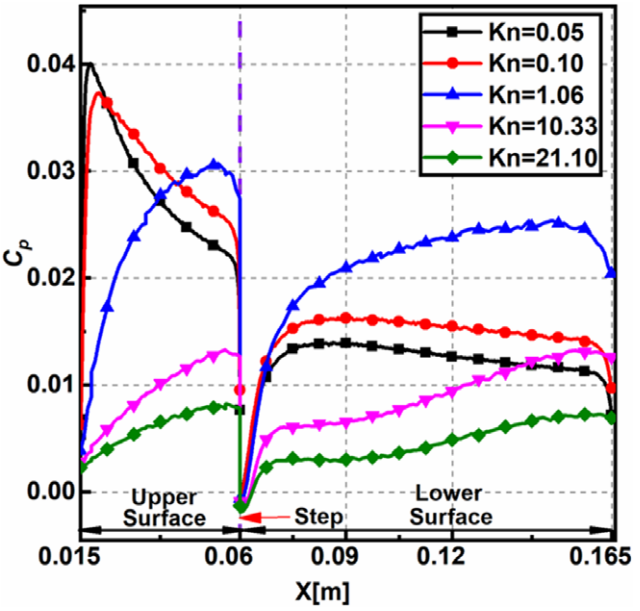

Figure 17. *Variation of pressure coefficient C_p on the upper and lower surfaces for various Kn.*

where, p_w denotes pressure at the wall, U_∞ is the free-stream velocity, p_∞ the free-stream pressure, and ρ_∞ the free-stream density, respectively.

The profiles adopt similar patterns in the slip regime for $Kn = 0.05, 0.10$, and another common trend in the transitional and free-molecular regime for $Kn = 1.06, 10.33$ and 21.10. The pressure coefficient demonstrates different trends in different rarefaction regimes, the change being observed from $Kn = 1.06$ onwards. The pressure coefficient C_p on the upper surface increases along the BFS length; however, there is a sudden peak in the slip regime compared to the transitional and free-molecular regime where the C_p gradually increases. The early peaks in the slip regime can be attributed to the higher near-wall pressure arising from the stagnation pressure rise of the fluid stream (Fig. 12). The peak C_p on the upper surface is observed at X locations of 0.01775, 0.0202, 0.05385, 0.05585 and 0.05595 for Kn 0.05, 0.1, 1.06, 10.33 and 21.10, respectively. Also, near the step, the magnitudes of C_p are below zero, owing to recirculation, which reduces the wall pressure below the free-stream value. The C_p on the lower surface behaves relatively similar for all cases, where the C_p increases and diminishes towards the outlet in the slip regime, whereas in the transitional and free-molecular regimes the C_p shows a gradually increasing trend. Furthermore, for all the cases, the magnitudes C_p near the outlet are greater than zero signifying a net higher near-wall pressure compared to free-stream pressure.

4.2.2 Skin friction coefficient

The skin friction coefficient (C_f) distribution for various Kn on the upper and the lower surfaces of the BFS is shown in Fig. 18. C_f is given by

$$C_f = \frac{\tau_w}{\frac{1}{2}\rho_\infty U_\infty^2} \tag{10}$$

where, τ_w denotes the shear stress at the wall, U_∞ is the free-stream velocity, and ρ_∞ the free-stream density.

Figure 18 shows larger values of C_f on the upper surface at the inlet owing to the substantial velocity gradients near the wall and progressively shows a decline after that. Also, the C_f increases with increase in the Knudsen number. In addition, the magnitudes of C_f show a significant jump for $Kn \geq 10.33$.

https://doi.org/10.1017/aer.2021.88 Published online by Cambridge University Press

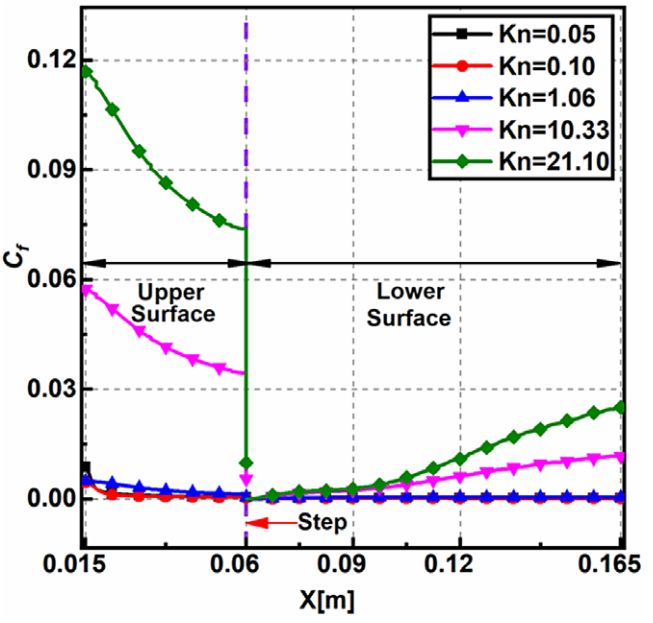

Figure 18. *Variation of skin friction coefficient C_f on the upper and lower surfaces for various Kn.*

For instance, the C_f at inlet almost doubles as *Kn* increases from 10.33 to 21.10. The magnitude of C_f show negative values close to the step owing to flow recirculation. On the lower surface, C_f for different *Kn* rises gradually towards the outlet. The C_f is reasonably same for $Kn \leq 1.06$, whereas it gradually increases for other cases. From Equation (2), as *Kn* increases, *Re* diminishes causing the viscous forces to dominate compared to the inertial forces, which leads to an increase in shear stress and C_f. At ($X = 60$mm) the peak values of C_f is found to be 4.38×10^{-4}, 3.30×10^{-4}, 5.60×10^{-4}, 5.29×10^{-3} and 9.56×10^{-3} for *Kn* 0.05, 0.1, 1.06, 10.33 and 21.10, respectively.

4.2.3 Heat transfer coefficient

The heat transfer coefficient (C_h) distribution for various *Kn* on the upper and the lower surfaces of the BFS is shown in Fig. 19. C_h is given by

$$C_h = \frac{q_w}{\frac{1}{2}\rho_\infty U_\infty^3} \tag{11}$$

where, q_w represents the heat flux at the wall, U_∞ is the free-stream velocity, and ρ_∞ denotes the free-stream density.

The plots of C_h and C_p are similar in appearance. Also, on the upper surface, the profiles are dissimilar for different *Kn*. Along the upper surface of the BFS, the heat transfer coefficient C_h show a sudden peak for $Kn \leq 0.10$, whereas a gradually increasing trend is observed in the other regimes. The peak C_h on the upper surface is observed at X locations 0.01615, 0.01745, 0.02085, 0.05575 and 0.05595 for *Kn* 0.05, 0.1, 1.06, 10.33 and 21.10, respectively. Near the base of the step, because of flow expansion, the temperature reduces, causing a drop in the heat transfer coefficient C_h. Along the lower surface the C_h values are relatively constant in the slip regime, showing a gradual increase in the higher rarefaction regimes. As the rarefaction increases, molecules present in the central domain participate in the collisions due to the increased mean free path, causing a rise in the heat transfer coefficient. Also, higher near-wall temperatures owing to viscous heating make the C_h magnitudes positive.

https://doi.org/10.1017/aer.2021.88 Published online by Cambridge University Press

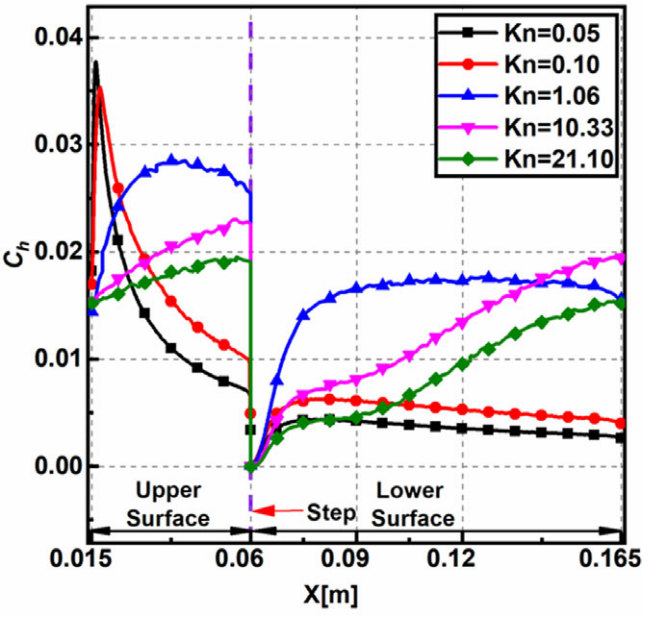

Figure 19. *Variation of heat transfer coefficient C_h on the upper and lower surfaces for various Kn.*

4.3 Comparison with chemically reacting flows

The flow conditions analysed in the present study are hypersonic, making the system energised, leading to the activation of the vibrational modes of the gas. Therefore, a comparative study is conducted between the reacting and non-reacting flows to demonstrate the differences observed when accounting for the chemical reactions.

The flow-field properties such as velocity, pressure and density showed no marked difference when compared against the non-reacting flows. Hence only the temperature field will be discussed in detail. The non-dimensional temperature contours for different components of the temperature $M = 25$ and $Kn = 1.06$ are shown in Fig. 20. Figure 20(a) shows that the vibrational component of the temperature, which is relatively lower in magnitude compared to the other components. In the wake of the step, the excitations remain unaffected, and as such, no marked difference is observed in the vibrational temperature. However, towards the outlet, there is a temperature surge.

Figure 20(b) shows that the rotational component of the temperature, which is of the same order as that of the vibrational component; however, the magnitudes are marginally higher. Figure 20(c) and (d) show the overall and translational components of the temperature, respectively. The contours show that the translational temperature near the wall is much greater than the temperature imposed at the wall and is of the order of 10^3K. This difference can be attributed to the viscous dissipation effects seen in the shear layer at the step height and near the wall. Similar behaviour is observed for rotational and vibrational temperatures as well. The combined effect is conveyed in the overall temperature contour in Fig. 20(c). Just upstream of the step, the flow begins to expand rapidly. This results in expansion cooling in the vicinity of the step and lower translational and rotational temperature values, as seen from the cold region behind the step. Furthermore, the effects of expansion cooling are also observed downstream near the outlet to reduce the translational temperature. Near the outlet, the high translational temperature in the shear layer downstream of the step reduces due to diffusion, advection, and reduced shear rates. Contrastingly, the rotational and vibrational temperatures are significantly amplified near the outlet due to the non-equilibrium effects, as seen in Fig. 20(a) and (b). The combined effect of this behaviour is reflected in the overall temperature with a relatively uniform temperature variation downstream of the

https://doi.org/10.1017/aer.2021.88 Published online by Cambridge University Press

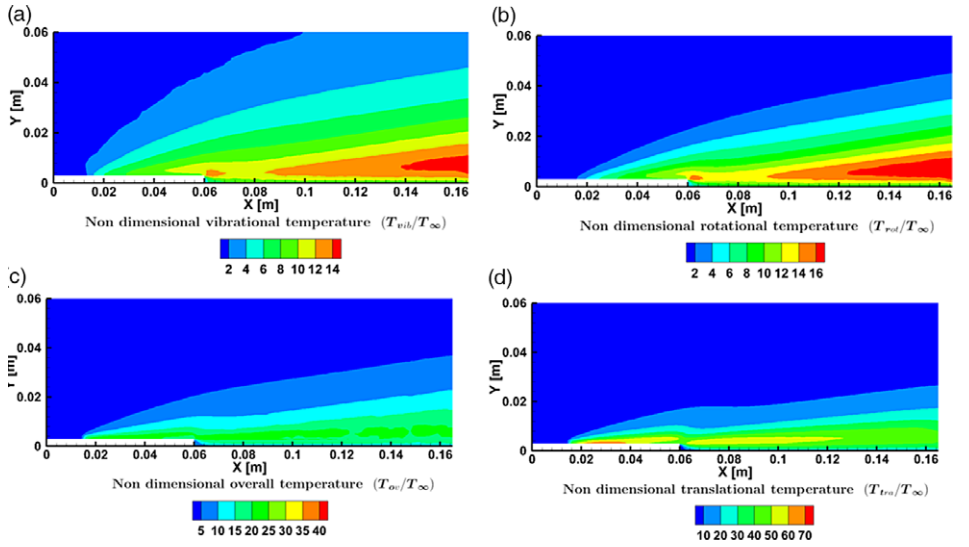

Figure 20. *Contours of non-dimensional (a) vibrational, (b) rotational, (c) overall and (d) translational temperature for* $M = 25$ *and* $Kn = 1.06$.

step, where the decreased translational temperature is compensated by the combined effect of increased rotational and vibrational temperature.

Figure 21(a–d) compares the temperature profiles normalised with the freestream temperature at different X locations. The temperature profiles for both chemically reacting flow as well as non-reacting flow are compared with each other. In all the chemically reacting flow plots, the temperature observed near the wall is an order higher than the imposed wall temperature. Even greater temperature values are observed at the step height in the shear layer due to viscous dissipation. Except for $X = 61$mm, the wall's temperature ratio increases with rarefaction. At higher Kn, viscous heat generation is dispersed over fewer molecules, thereby resulting in a more significant temperature increment. At the middle of the flow domain, $Y = 30$mm, the temperature again rises with rarefaction. The general trend observed along the Y direction, away from the wall, is the rapid increase in temperature until it attains a maximum value. It then follows a gradual decrease in the temperature ratio until the ratio equals one.

When the results are compared with the non-reacting flow, a considerable difference is observed. At $X = 30$mm the wall temperature ratio values predicted by non-reacting flow, differ with chemically reacting flow by roughly 78%, 109%, 57.2%, 0.49% and −5.7% for $Kn = 0.05, 0.10, 1.06, 10.33$ and 21.10, respectively. Similarly, just upstream of the step at $X = 59$mm, the wall temperatures differ by 50.8%, 67.6%, 71%, 16.7% and 5.2% for $Kn = 0.05, 0.10, 1.06, 10.33$ and 21.10, respectively, with respect to the chemically reacting flow. Finally, at $X = 120$mm, the error in the wall temperature ratio is between 18% and 19% for all degrees of rarefaction.

At all X locations, the free molecular flow shows a good agreement with the results predicted by the non-reacting flow. Furthermore, the maximum temperature in the shear layer also is calculated and the error is measured with the non-reacting flow at various locations. At $X = 30$mm the maximum temperature ratio values predicted by non-reacting flow, differ with chemically reacting flow by roughly 72%, 88.9%, 57.2%, 0.49% and −5.7% for $Kn = 0.05, 0.10, 1.06, 10.33$ and 21.10, respectively. At $X = 59$mm, the percentage error is 46.9%, 57.8%, 88.7%, 16.7%, and 5.2% for $Kn = 0.05, 0.10, 1.06, 10.33$ and 21.10, respectively. Downstream of the step, the error in the maximum temperature is greater than 40% for all Kn at $X = 61$ and 120mm.

https://doi.org/10.1017/aer.2021.88 Published online by Cambridge University Press

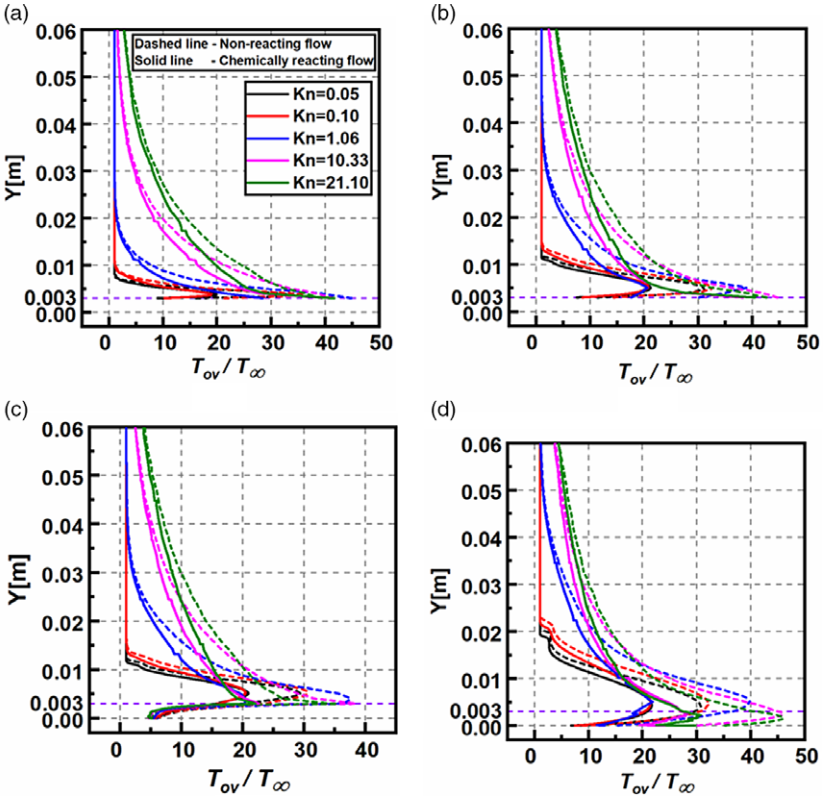

Figure 21. *Comparison of the non-dimensional overall temperature for various Kn at (a)* $X = 30$mm*, (b)* $X = 59$mm*,(c)* $X = 61$mm *and (d)* $X = 120$mm *for reacting and non-reacting cases.*

5.0 Conclusion

The BFS can be approximated as one of the abnormalities that can occur on the surface of a hypersonic vehicle, the study of which aids in the understanding of the flow dynamics over such vehicles. Thus, this study explores the various loads encountered by a re-entry vehicle passing through different altitudes covering different rarefaction regimes. The DSMC method is used as a numerical tool to conduct the studies. The numerical model is validated with the literature results, and a good agreement is found among them. The investigations were performed to analyse the rarefaction effects on the flow-field and aerodynamic properties. The main conclusions are listed as follows:

1. The non-dimensional velocity assumed a non-zero value at the walls, which differs from the traditional continuum approach. Also, the boundary layer thickness increased significantly with rarefaction. Furthermore, the near wall slip also showed an increase with rarefaction.
2. Near the downstream of the step, flow recirculation was observed in all regimes. The recirculation lengths decreased with increasing *Kn*, which can be attributed to the domination of viscous forces.
3. The non-dimensional pressure and temperature showed identical behaviour with higher magnitudes near the walls and decreased magnitude away from the wall in the perpendicular direction. Also, the rarefaction effects caused an increase in the magnitudes of both the pressure and temperature in the domain due to viscous dissipation and compressibility effects.

https://doi.org/10.1017/aer.2021.88 Published online by Cambridge University Press

4. The different components of the temperature showed similar behaviour with increasing magnitudes with an increase in *Kn*. However, the change in the rotational component was noticeable only in the lower rarefaction regimes.
5. The temperature jump showed a sudden rise along the flow direction, succeeded by a gradual decrease in the slip and transitional regime. In contrast, in the free-molecular regime, the temperature jump showed a gradual increase.
6. The non-dimensional density, owing largely to the compressibility of the flow, showed significant changes in the slip regime, whereas minimal variation was found in the other regimes.
7. The aerodynamic surface properties C_p and C_h by and large followed a similar trend, with peak magnitudes located upstream. The skin friction coefficient C_f on the other hand, showed a consistent increase with *Kn* all along the lower and upper surfaces. Also, C_f increased continuously with the distance from the step.
8. The flow-field properties such as velocity, pressure and density showed no marked difference when compared against the non-reacting flows, whereas considerable variation was observed in the temperature field.

The previous trends give a detailed analysis of the rarefaction effects on the hypersonic flow past BFS and offer valuable insights into the flow characteristics of the cases considered.

References

[1] Guo, G. and Luo, Q. Flowfield structure characteristics of the hypersonic flow over a cavity: From the continuum to the transition flow regimes, *Acta Astronaut.*, 2019, **161**, pp 87–100.
[2] Gallis, M.A. Bond, R.B. and Torczynski, J.R. A kinetic-theory approach for computing chemical-reaction rates in upper-atmosphere hypersonic flows, *J. Chem. Phys.* 2009, **131**, (12), p 124311.
[3] Palharini, R.C. Scanlon, T.J. and Reese, J.M. Aerothermodynamic comparison of two- and three-dimensional rarefied hypersonic cavity flows, *J. Spacecr. Rockets*, Sep. 2014, **51**, (5), pp 1619–1630, doi: 10.2514/1.A32746.
[4] Morgan, K. Periaux, J. and Thomasset, F. *Analysis of Laminar Flow Over a Backward Facing Step*. Springer, 1984.
[5] Chen, L. Asai, K. Nonomura, T. Xi, G. and Liu, T. A review of backward-facing step (BFS) flow mechanisms, heat transfer and control, *Ther. Sci. Eng. Prog.* 2018, **6**, pp 194–216.
[6] Leite, P.H.M. and Santos, W.F.N. Computational Analysis of a Rarefied Hypersonic Flow over Backward-Facing Steps, *J. Thermophys. Heat Transf.*, Feb. 2019, pp 1–13, doi: 10.2514/1.T5486.
[7] Ahmadian, M.H. Roohi, E. Teymourtash, A. and Stefanov, S. A dusty gas model-direct simulation Monte Carlo algorithm to simulate flow in micro-porous media, *Phys. Fluids*, Jun. 2019, **31**, (6), p 062007, doi: 10.1063/1.5094637.
[8] Mohammadzadeh, A. Roohi, E. Niazmand, H. Stefanov, S. and Myong, R.S. Thermal and second-law analysis of a micro- or nanocavity using direct-simulation Monte Carlo, *Phys. Rev. E Stat. Nonlin. Soft Matter Phys.* May 2012, **85**, (5 Pt 2), p 056310, doi: 10.1103/PhysRevE.85.056310.
[9] Choi, H. Lee, D. and Lee, D. Complex microscale flow simulations using langmuir slip condition, *Numer. Heat Transf. A Appl.* Sep. 2005, **48**, (5), pp 407–425, doi: 10.1080/10407780590957206.
[10] Hsieh, T.-Y. Hong, Z.-C. and Pan, Y.-C. Flow characteristics of three-dimensional microscale backward-facing step flows, *Numer. Heat Transf. A Appl.* Mar. 2010, **57**, no. 5, pp 331–345, doi: 10.1080/10407780903582992.
[11] Beskok, A. Validation of a new velocity-slip model for separated gas microflows, *Numer. Heat Transf. B Fundam.* Dec. 2001, **40**, (6), pp 451–471, doi: 10.1080/104077901753306593.
[12] Celik, B. and Edis, F.O. Computational investigation of micro bacward-facing step duct flow in slip regime, *Nanoscale Microscale Thermophys. Eng.* Dec. 2007, **11**, (3–4), pp 319–331, doi: 10.1080/15567260701715438.
[13] Rached, J.A. and Daher, N.M. *Numerical Prediction of Slip Flow and Heat Transfer in Microchannels*, 2007, pp 109–114.
[14] Baysal, O. Erbas, N. and Koklu, M. Control of separated flow past a backward facing step in a microchannel, *Microfluid. Nanofluid.* Nov. 2004, **1**, (1), pp 86–92, doi: 10.1007/s10404-004-0003-x.
[15] Xue, H. and Chen, S. DSMC simulation of microscale backward-facing step flow, *Microscale Thermophys. Eng.* Jan. 2003, **7**, (1), pp 69–86, doi: 10.1080/10893950390150449.
[16] Nabapure, D. and Kalluri, R.C.M. DSMC simulation of rarefied gas flow over a 2D backward-facing step in the transitional flow regime: Effect of Mach number and wall temperature, *Proc. Inst. Mech. Eng. G J. Aerosp. Eng.*, 2020, p. 0954410020959872.
[17] Kursun, U. and Kapat, J.S. Modeling of microscale gas flows in transition regime Part I: Flow over backward facing steps, *Nanoscale Microscale Thermophys. Eng.* May 2007, **11**, (1–2), pp 15–30, doi: 10.1080/15567260701333372.
[18] Bao, F. and Lin, J. Continuum simulation of the microscale backward-facing step flow in a transition regime, *Numer. Heat Transf. A Appl.* Apr. 2011, **59**, (8), pp 616–632, doi: 10.1080/10407782.2011.561073.

https://doi.org/10.1017/aer.2021.88 Published online by Cambridge University Press

[19] Darbandi, M. and Roohi, E. DSMC simulation of subsonic flow through nanochannels and micro/nano backward-facing steps, *Int. Commun. Heat Mass Transf.* Dec. 2011, **38**, (10), pp 1443–1448, doi: 10.1016/j.icheatmasstransfer.2011.08.002.

[20] Mahdavi, A.-M. and Roohi, E. Investigation of cold-to-hot transfer and thermal separation zone through nano step geometries, *Phys. Fluids*, , Jul. 2015, **27**, (7), p 072002, doi: 10.1063/1.4927069.

[21] Mahdavi, A.-M. Le, N.T.P. Roohi, E. and White, C. Thermal rarefied gas flow investigations through micro-/nano-backward-facing step: Comparison of DSMC and CFD subject to hybrid slip and jump boundary conditions, *Numer. Heat Transfer A Appl.* Oct. 2014, **66**, (7), pp 733–755, doi: 10.1080/10407782.2014.892349.

[22] Gavasane, A. Agrawal, A. and Bhandarkar, U. Study of rarefied gas flows in backward facing micro-step using Direct Simulation Monte Carlo, *Vacuum*, Sep. 2018, **155**, pp 249–259, doi: 10.1016/j.vacuum.2018.06.014.

[23] Guo, G. Liu, H. and Zhang, B. Numerical study of active flow control over a hypersonic backward-facing step using supersonic jet in near space, *Acta Astronaut.* Mar. 2017, **132**, pp 256–267, doi: 10.1016/j.actaastro.2016.12.035.

[24] Paolicchi, L.T.L.C. and Santos, W.F.N. Length-to-depth ratio effects on aerodynamic surface quantities of a hypersonic gap flow, *AIAA J.* Feb. 2018, **56**, (2), pp 780–792, doi: 10.2514/1.J055826.

[25] Guo, G. and Luo, Q. DSMC investigation on flow characteristics of rarefied hypersonic flow over a cavity with different geometric shapes, *Int. J. Mech. Sci.* Nov. 2018, **148**, pp 496–509, doi: 10.1016/j.ijmecsci.2018.09.022.

[26] Palharini, R.C. and Santos, W.F. The impact of the length-to-depth ratio on aerodynamic surface quantities of a rarefied hypersonic cavity flow, *Aerosp. Sci. Technol.* 2019, **88**, pp 110–125.

[27] Jin, X. Wang, B. Cheng, X. Wang, Q. and Huang, F. The effects of Maxwellian accommodation coefficient and free-stream Knudsen number on rarefied hypersonic cavity flows, *Aerosp. Sci. Technol.* Feb. 2020, **97**, p 105577, doi: 10.1016/j.ast.2019.105577.

[28] Bird, G.A. *Molecular Gas Dynamics and the Direct Simulation of Gas Flows,* Oxford University Press, New York, 1994.

[29] Zhang, B. Liu, H. and Jin, S. An asymptotic preserving Monte Carlo method for the multispecies Boltzmann equation, *J. Computat. Phys.* 2016, **305**, pp 575–588.

[30] Roohi, E. and Stefanov, S. Collision partner selection schemes in DSMC: From micro/nano flows to hypersonic flows, *Phys. Rep.* Oct. 2016, **656**, pp 1–38, doi: 10.1016/j.physrep.2016.08.002.

[31] Roohi, E. Stefanov, S. Shoja-Sani, A. and Ejraei, H. A generalized form of the Bernoulli Trial collision scheme in DSMC: Derivation and evaluation, *J. Computat. Phys.* Feb. 2018, **354**, pp 476–492, doi: 10.1016/j.jcp.2017.10.033.

[32] Abe, T. Generalized scheme of the no-time-counter scheme for the DSMC in rarefied gas flow analysis, *Comput. Fluids*, Mar. 1993, **22**, (2), pp 253–257, doi: 10.1016/0045-7930(93)90057-G.

[33] Prasanth, P. and Kakkassery, J.K. Molecular models for simulation of rarefied gas flows using direct simulation Monte Carlo method, *Fluid Dyn. Res.* 2008, **40**, (4), p 233.

[34] Alexander, F.J. Garcia, A.L. and Alder, B.J. Cell size dependence of transport coefficients in stochastic particle algorithms, *Phys. Fluids*, May 1998, **10**, (6), pp 1540–1542, doi: 10.1063/1.869674.

[35] Hadjiconstantinou, N.G. Analysis of discretization in the direct simulation Monte Carlo, *Phys. Fluids*, Sep. 2000, **12**, (10), pp 2634–2638, doi: 10.1063/1.1289393.

[36] Scanlon, T.J. Roohi, E. White, C. Darbandi, M. and Reese, J.M. An open source, parallel DSMC code for rarefied gas flows in arbitrary geometries, *Comput. Fluids*, Dec. 2010, **39**, (10), pp 2078–2089, doi: 10.1016/j.compfluid.2010.07.014.

[37] White, C. et al. dsmcFoam+: An OpenFOAM based direct simulation Monte Carlo solver, *Comput. Phys. Commun.* Mar. 2018, **224**, pp 22–43, doi: 10.1016/j.cpc.2017.09.030.

[38] US Standard Atmosphere, *US Standard Atmosphere*. National Oceanic and Atmospheric Administration, 1976.

[39] Leite, P.H.M. and Santos, W.F.N. Computational analysis of the flow field structure of a non-reacting hypersonic flow over forward-facing steps, *J. Fluid Mech.* Jan. 2015, **763**, pp 460–499, doi: 10.1017/jfm.2014.677.

[40] Bird, G.A. Simulation of multi-dimensional and chemically reacting flows (past Space Shuttle orbiter), *Rarefied Gas Dyn.*, 1979, pp 365–388.

[41] Bird, G.A. The Q-K model for gas-phase chemical reaction rates, *Phys. Fluids*, 2011, doi: 10.1063/1.3650424.

[42] Bird, G. *Molecular Gas Dynamics and the Direct Simulation Monte Carlo of Gas Flows*, Clarendon, Oxford, **508**, p. 128, 1994.

[43] Nabapure, D. Sanwal, J. Rajesh, S. and Murthy, K.R.C. Investigation of Subsonic and Hypersonic Rarefied Gas Flow over a Backward Facing Step, *J. Phys. Conf. Ser.* 2019, 1276, p 012007.

[44] Nabapure, D. and Kalluri, R. DSMC investigation of rarefied gas flow over a 2D forward-facing step: Effect of Knudsen number, *Acta Astronaut.* Jan. 2021, **178**, pp 89–109, doi: 10.1016/j.actaastro.2020.08.030.

[45] Nabapure, D. and Ram Chandra Murthy, K. Simulation of flow in single and double-sided lid driven square cavities by direct simulation Monte Carlo method, *Thermal Science*, 2020, **24**, (5 Part A), pp 3031–3045, doi: 10.2298/TSCI180906066N.

[46] Nabapure, D. and Kalluri, R.C.M. DSMC simulation of rarefied gas flow over a forward-facing step, *ICTEA: International Conference on Thermal Engineering*, 2019.

[47] Nabapure, D. and Ram Chandra Murthy, K. Investigation of Rarefied Open Cavity Flows in all Rarefaction Regimes using DSMC Method, in APS Division of Fluid Dynamics Meeting Abstracts, 2020, pp K18-005.

[48] Nabapure, D. et al. DSMC investigation of rarefied gas flow in a four-sided lid driven cavity: Effect of rarefaction and lid velocities, *Journal of Computational Science*, **49**, p. 101276, 2021.

[49] Nabapure, D. Singh, A. and Murthy, K.R.C. Effect of Mach Number on the rarefied gas flow over a forward-facing step, *Theoretical, Computational, and Experimental Solutions to Thermo-Fluid Systems: Select Proceedings of ICITFES 2020*, p. 451.

[50] Nabapure, D. and Murthy, R.C. DSMC simulation of rarefied gas flow over a wall mounted cube, *Fluids Engineering Division Summer Meeting*, 2019, 59032, p V002T02A071.

https://doi.org/10.1017/aer.2021.88 Published online by Cambridge University Press

[51] Nabapure, D. and Murthy, K.R.C. DSMC simulation of rarefied gas flow over a forward-facing step: Effect of expansion ratio, *AIP Conf. Proc.* 2021, **2316**, (1), p 030032.
[52] Scanlon, T.J. et al. Open-source direct simulation monte carlo chemistry modeling for hypersonic flows, *AIAA J.* 2015, **53**, (6), pp 1670–1680.
[53] Karchani, A. and Ejtehadi, O. A review and perspective on a convergence analysis of the direct simulation Monte Carlo and solution verification, *Phys. Fluids*, Jun. 2019, **31**, (6), p 066101, doi: 10.1063/1.5093746.
[54] Grotowsky, I.M.G. and Ballmann, J. Numerical investigation of hypersonic step-flows, *Shock Waves*, Mar. 2000, **10**, (1), pp 57–72, doi: 10.1007/s001930050179.
[55] Ejtehadi, O. Roohi, E. and Esfahani, J.A. Detailed investigation of hydrodynamics and thermal behavior of nano/micro shear driven ow using DSMC, *Sci. Iran.*, 2013, p 13.
[56] Schäfer, F. Breuer, M. and Durst, F. The dynamics of the transitional flow over a backward-facing step, *J. Fluid Mech.*, Mar. 2009, **623**, p 85, doi: 10.1017/S0022112008005235.
[57] Deepak, N. Gai, S. and Neely, A. A computational study of high enthalpy flow over a rearward facing step, *48th AIAA Aerospace Sciences Meeting Including the New Horizons Forum and Aerospace Exposition*, Orlando, FL, AIAA Paper, 2010, p. 444.
[58] Balaj, M. Akhlaghi, H. and Roohi, E. Rarefied gas flow behavior in micro/nanochannels under specified wall heat flux, *Int. J. Mod. Phys. C*, Aug. 2015, **26**, (08), p 1550087, doi: 10.1142/S0129183115500874.
[59] Hong, C. and Asako, Y. Some considerations on thermal boundary condition of slip flow, *Int. J. Heat Mass Transf.* 2010, **53**, (15–16), pp 3075–3079.

Cite this article: Nabapure D., Singh A. and Kalluri R.C.M. (2022). Investigation of rarefied flow over backward-facing step in different rarefaction regimes using direct simulation Monte Carlo. *The Aeronautical Journal*, **126**, 617–644. https://doi.org/10.1017/aer.2021.88